



저작자표시-비영리-변경금지 2.0 대한민국

이용자는 아래의 조건을 따르는 경우에 한하여 자유롭게

- 이 저작물을 복제, 배포, 전송, 전시, 공연 및 방송할 수 있습니다.

다음과 같은 조건을 따라야 합니다:



저작자표시. 귀하는 원저작자를 표시하여야 합니다.



비영리. 귀하는 이 저작물을 영리 목적으로 이용할 수 없습니다.



변경금지. 귀하는 이 저작물을 개작, 변형 또는 가공할 수 없습니다.

- 귀하는, 이 저작물의 재이용이나 배포의 경우, 이 저작물에 적용된 이용허락조건을 명확하게 나타내어야 합니다.
- 저작권자로부터 별도의 허가를 받으면 이러한 조건들은 적용되지 않습니다.

저작권법에 따른 이용자의 권리는 위의 내용에 의하여 영향을 받지 않습니다.

이것은 [이용허락규약\(Legal Code\)](#)을 이해하기 쉽게 요약한 것입니다.

[Disclaimer](#)

공학박사학위논문

**In-silico simulation based multiscale wafer
fracture model considering the uncertainty of
material properties**

재료의 불확실성을 고려한 인실리코 해석 기반
멀티스케일 웨이퍼 파괴 모델

2021년 8월

서울대학교 대학원

기계항공공학부

정 인 균

**In-silico simulation based multiscale wafer
fracture model considering the uncertainty of
material properties**

**재료의 불확실성을 고려한 인실리코 해석 기반
멀티스케일 웨이퍼 파괴 모델**

지도교수 조 맹 효

이 논문을 공학박사 학위논문으로 제출함

2021 년 4 월

서울대학교 대학원

기계항공공학부

정 인 균

정인균의 공학박사 학위논문을 인준함

2021 년 6 월

위원장 : 김 윤 영

부위원장 : 조 맹 효

위 원 : 윤 병 동

위 원 : 김 도 년

위 원 : 양 승 화

Abstract

In this dissertation, a statistical wafer fracture model is proposed to characterize the fracture behavior of laminated wafer structure, considering uncertainties of material and interfacial bonding conditions. During the manufacturing process, a wafer film is exposed to a variety of external environments such as repeating heating cycle process, substrate oxidation, and X-ray exposure. Due to these external factors, various interfacial breakage phenomena are observed in the wafer substrate for which it is difficult to know the reason of failure. Thus, it is important to identify the fracture mechanism of the wafer film, also the failure rate of wafer film has been considerable problem during in semiconductor industry. However, there are several limitations to experimental tests for fracture analysis of wafer film. Therefore, many studies have been conducted to analyze the phenomenon of wafer fracture based on computer simulation, and in particular, fracture analysis has been mainly conducted through the cohesive zone model. However, it is difficult to accurately simulate the interfacial bonding conditions observed at the nanoscale because the existing analysis model is built based on experimental data at the macro scale. In addition, the thickness of laminated wafer structure is very thin, so each layered structure is a nano-scale structure, and thus the material constituting the wafer is non-uniformly formed. As a result, uncertainties in the physical properties of wafer materials arise, and uncertainties in the interfacial properties between materials also occur. The material uncertainty has a great effect

on the destruction of the entire wafer structure, so it is necessary to analyze the fracture analysis of wafer film considering these uncertainties. Also statistical-based fracture analysis considering those uncertainties is a dominant issue that is being studied recently in various composite materials such as concrete and polymer composite materials as well as wafer structure.

In this study, a statistical-based molecular dynamics analysis model is introduced to solve the uncertainties of material and interfacial properties at the nano-scale. Through those statistical analysis, the thermo-mechanical properties of wafer materials and interfacial fracture properties can be expressed based on a normal distribution. Also it is possible to newly propose the statistical fracture criterion at the interface of laminated wafer structure through Monte-Carlo simulations. The probability distribution of those properties are calculated considering the uncertainties of wafer material and interfacial characteristics through molecular dynamics simulations. Based on those distributions, a finite element fracture model is constructed through the cohesive zone model. The cohesive zone model is characterized by using statistical multiscale bridging method to reflect the uncertainties of material and interfacial properties for wafer film. In order to consider those statistical-based properties together, in this study, a Monte-Carlo simulations are performed and a statistical-based fracture analysis model is newly suggested. Statistical-based numerical results provide not only numerical solutions with reliability bounds in continuum scale but also error range and failure rate of the wafer system.

The most commonly used 3D plate model is constructed as simulation model of laminated wafer structure, and the statistical-based model is compared with conventional wafer fracture models such as perfect bonding model and cohesive zone model based simple power-law criterion. The degree of deformation and fracture behavior under thermal stress for each wafer fracture model are compared. Statistical wafer fracture model can present analysis values in the form of a normal distribution, and through this, the yield rate of laminated wafer structure can be predicted unlike other models. Furthermore, it is confirmed that the proposed model can more accurately investigate the fracture analysis of wafer film than those existing models through comparison with experimental data.

Keywords

Multiscale simulations, Molecular dynamics simulations, Statistical fracture analysis, Continuum analysis, laminated wafer structure

Student Number : 2014-22473

Contents

| | |
|--|-------------|
| Abstract | i |
| Contents | iii |
| List of figures | vi |
| List of tables | viii |
| | |
| Chapter 1 Introduction | 1 |
| | |
| Chapter 2 Wafer Fracture Model Considering Uncertainty | 11 |
| 2.1 MD Model Considering Uncertainty | 11 |
| 2.2 Traction-Separation Curves for Fracture Modes | 13 |
| 2.3 Statistical Mixed-Mode Fracture Criterion | 15 |
| 2.4 Wafer Fracture Model by Multi-Scale Simulations..... | 18 |
| | |
| Chapter 3 Applications of Statistical Wafer Fracture Model..... | 39 |
| 3.1 Statistical Multi-Scale Modeling for Wafer Film | 39 |
| 3.2 Comparison Proposed Model with Conventional Model | 41 |
| | |
| Chapter 4 Conclusions | 54 |

| | |
|---|------------|
| Appendix A. Traction-Separation Curves by MD simulations..... | 57 |
| A.1 Overview | 57 |
| A.2 Traction-Separation for Temperature and Tensile Rate | 58 |
| A.3 Characterization of Mixed-Mode Cohesive Law | 62 |
| Appendix B. Effective Thickness of Cohesive Zone Element | 72 |
| B.1 Overview..... | 72 |
| B.2 Interface Slab Length Effect for Bi-Layer Model..... | 73 |
| B.3 Effective Thickness of Cohesive Zone Element..... | 80 |
| Appendix C. Stochastic Neural Network Constitutive Model..... | 84 |
| C.1 Overview..... | 84 |
| C.2 Statistical Stress-Strain Responses of Polymer Material | 85 |
| C.3 Verification of Machine-Learning Function | 90 |
| C.4 Numerical Examples of NN Stochastic Constitutive Model ... | 93 |
| C.5 Summary..... | 95 |
| Bibliography..... | 96 |
| 국문 요약..... | 102 |

List of figures

| | |
|---|----|
| Figure 2.1 All-atom model of (a) SOH polymer and (b) SiN | 21 |
| Figure 2.2 Probability distribution of modulus and CTE | 22 |
| Figure 2.3 Bi-layer model of SiN/SOH traction-separation model | 23 |
| Figure 2.4 Schematic diagram of fracture simulations | 23 |
| Figure 2.5 T-S data for normal mode with different number of data sets. | 24 |
| Figure 2.6 T-S data for shear mode with different number of data sets.... | 24 |
| Figure 2.7 Standard deviation of T, K, and G for normal mode according to # of data points | 25 |
| Figure 2.8 T-S data sets for (a) normal mode and (b) shear mode by MD simulations..... | 26 |
| Figure 2.9 Normal distribution curves for normal mode | 27 |
| Figure 2.10 Normal distribution curves for shear mode..... | 28 |
| Figure 2.11 Correlation between T, K, G for normal mode..... | 29 |
| Figure 2.12 Correlation between T, K, G for shear mode..... | 30 |
| Figure 2.13 Statistical T-S curves for (a) normal mode and (b) shear mode by MD simulations | 31 |
| Figure 2.14 Schematic flow for statistical fracture criterion | 32 |
| Figure 2.15 Statistical fracture criterion based on normal distribution | 33 |

| | |
|---|----|
| Figure 2.16 Statistical mixed-mode cohesive law based on a normal distribution..... | 34 |
| Figure 2.17 Schematic flow for step 1 of constructing the wafer fracture model | 35 |
| Figure 2.18 Schematic flow for step 2 of constructing the wafer fracture model | 36 |
| Figure 3.1 Schematic diagram of 3D plate model | 45 |
| Figure 3.2 3D plate model of (a) undeformed state and (b) deformed state from 0K to 800K | 46 |
| Figure 3.3 3D plate model of (a) undeformed state and deformed state for (b) perfect bonding model, (c) cohesive zone model and (d) statistical fracture model | 47 |
| Figure 3.4 3D plate model of (a) undeformed state and (b) deformed state of SDEG distribution | 49 |
| Figure 3.5 SDEG distribution comparison statistical model with cohesive zone model..... | 50 |
| Figure 3.6 Reference data of (a) Polymer-SiN substrate model and (b) Debond length according to temperature..... | 51 |
| Figure A.2.1 Fracture toughness curves according to (a) and (b) temperature, and (c) tensile rate [31,32]..... | 60 |
| Figure A.2.2 T-S curves for (a) temperatures and (b) tensile rates | 61 |

| | |
|--|----|
| Figure A.3.1 Schematic diagram of determining mode-mixity | 68 |
| Figure A.3.2 Determine mode mixity by power law criterion..... | 69 |
| Figure A.3.3 (a) Mixed mode cohesive law and its (b) T-S curves | 70 |
| Figure B.2.1 T-S curves for slab lengths of 2.5nm, 3.5nm, 5.5nm, 6.5nm, 7.5nm | 76 |
| Figure B.2.2 Schematic diagram for simple normal test | 77 |
| Figure B.2.3 Cohesive zone model for (a) stress distribution and (b) SDEG distribution..... | 78 |
| Figure B.3.1 Dissipation energy for (a) fixed CZ length and (b) effective CZ length | 82 |
| Figure C.2.1 MD data of (a) monotonic and (b) combined loading | 87 |
| Figure C.2.2 Normal distribution of the stress value with strain..... | 88 |
| Figure C.2.3 Stochastic data conversion process from (a) band gap data to (b) stochatsic data..... | 89 |
| Figure C.3.1 Additional combined loading conditions of 2-D and 3-D behaviors..... | 91 |
| Figure C.3.2 Comparation of MD data and learning data under the conditions indicated in (a), (b), (c), and (d) | 92 |

Figure C.4.1 Corner brace model: (a) schematic diagram and (b) deformed state of NN model..... 94

Figure C.4.2 Displacement distribution at point A and (b) stress distribution of the corner brace model..... 94

List of tables

| | |
|---|----|
| Table 2.1 Thermo-mechanical properties of SOH and SiN | 37 |
| Table 2.2 Normal distributions of thermo-mechanical properties for SOH and SiN | 37 |
| Table 2.3 Standard deviation of T, K, and G for each mode compared with reference data..... | 38 |
| Table 3.1 Deformation (U) of wafer fracture model for perfect bonding model, cohesive zone model, and statistical fracture model | 52 |
| Table 3.2 SDEG of wafer fracture model for perfect bonding model, cohesive zone model, and statistical fracture model | 52 |
| Table 3.3 Yield rate of wafer fracture model for perfect bonding model, cohesive zone model, and statistical fracture model | 54 |
| Table 3.4 Comparison of normalized debond length on wafer film among reference data and fracture models..... | 54 |
| Table A.3.1 Fracture properties for normal direction derived by MD | 71 |
| Table A.3.2 Fracture properties for shear direction derived by MD | 71 |
| Table B.2.1 Fracture properties for different slab lengths of 2.5nm, 3.5nm, 5.5nm, 6.5nm, and 7.5nm | 79 |
| Table B.3.1 Dissipation energy according to CZ length for slab length ... | 83 |

Chapter 1

Introduction

1.1 Fracture Issue in Laminated Wafer Structure in Semiconductor Industry

Semiconductor wafer is used as core parts of IT devices such as computers and smart phones, and applications of various materials or product developments are actively performed according to their demands [1]. In particular, the wafer manufacturing process of semiconductor wafers is quite complex and consists of several stages, so the manufacturing process is carried out at various scales from micro scale to macro scale. The main manufacturing process of the wafer film is composed of 10 steps as follows: Raw material selection, crystal growing, evaluation, slicing, lapping, etching, heat treatment, polishing, cleaning, inspection, packing,

and the wafer film is exposed to external environments such as x-ray radiation, oxidation, and thermal stress during those processes [2]. During those corresponding processes, failure behaviors in the wafer are investigated since the wafer structure is critically damaged due to those external stimuli. In particular, wafer structures undergo major temperature changes during those processes and a thermal stress derived by the temperature change is assumed to be a predominant cause of the wafer failure [3]. The wafer system is composed of several materials such as spin on hard mask (SOH) polymer, silicon nitride (SiN), silicon dioxide, and amorphous carbon according to its use, which is constructed as a laminated composite structure [4]. The repetitive process of removing membrane materials and stacking new materials are produced in the process of the wafer film. Accordingly, cracks or voids are generated on the interface of stacking materials during the process, which induces the structural damage to the wafer structure [5]. Therefore, it is a dominant issue in the production of wafer films that reducing a failure rate and identifying a cause of fracture propagation as the difficulty of the manufacturing process increases. Notably, the above fracture phenomenon occurs mainly in the interface of the wafer film due to its structural characteristics, so it is important to understand the interfacial failure characteristics of the wafer film under various combined loading conditions. However, there are few experimental research results about interfacial characteristics of wafer composite materials. Also there is a limit to implementing the interfacial fracture tests for each composite material because various materials are employed as a wafer material depending on where they are used. Moreover, it is difficult to

observe the interfacial failure in real time due to characteristics of the wafer process, which results in identifying difficult how structural failure occurs on wafer.

1.2 Previous Fracture Analysis in Wafer Film

The failure mechanism of laminated wafer structures have been implemented through computer simulation methodology to overcome those corresponding limitations of experiments. As computer simulation methodologies have been advanced, variety of analytical model techniques have been used to establish a failure model. Recently, a study on the construction of the damage model is focused on a cohesive zone model [6], which describes the fracture constitutive behavior and identifies the crack propagation and failure event near crack or void. Above all, the cohesive zone model has been considerably used to investigate the fracture analysis such as crack propagation [7], de-bonding effect [8], interface failure [9], and bulk failure [10], which describes the fracture constitutive behavior near crack or void. In addition, the model could be developed reflecting various external conditions and structural characteristics, so parametric studies based on those parameters such as crack initiation, void size, temperature, and material types could be easily implemented for different cases.

However, the existing wafer fracture model has been analyzed by constructing a cohesive zone model based on the material properties measured at the macro scale. Wang et al [11] construct a wafer fracture model assuming that the

interfacial bonding condition between wafer materials is perfect bonding condition, and based on this, observed the shear deformation of the wafer system. Reuther et al [12] calculated the interfacial properties in normal mode and shear mode through bending test of wafer composite material in macro scale, and then constructed a simple power-law criterion based on this to investigate a cohesive zone model. Through the wafer model, the phenomenon of wafer fracture due to bending in laminated composite structures was analyzed. Therefore, since previous wafer fracture analysis models are based on macro-scale-based experimental data, there is a limitation in that it is difficult to properly simulate the interfacial properties between wafer materials observed at the nano-scale. To solve this limitation, it is necessary to analyze the wafer fracture model at the nanoscale, and in particular, the interfacial bonding condition in the wafer material can be more accurately analyzed through MD simulations.

In order to determine the interfacial fracture properties in laminated composite materials, there are many studies that analyze them through MD simulations. Those fracture properties are calculated by traction-separation responses on the fracture area, which is determined according to fracture mode such as normal mode, shear mode, and transverse mode of the laminated composite system [13]. The normal mode is the failure analytical mode caused by vertical stress, also shear mode and transverse mode are defined as a failure mode by shear stress and transverse stress. But failure mechanisms on laminated composite structure are generally considered as a mixed mode fracture behavior, which is combined with

normal mode, shear mode, and transverse mode. Thus, many researches have been conducted to investigate the fracture propagation of laminated composite structure by using fracture mode analysis containing single mode and mixed mode. Besides, traction-separation responses on the interface of laminated composite structure are developed by those fracture mode analysis for each direction. Especially, the analytical research based MD simulations have been implemented by performing fracture tensile simulations to obtain traction-separation curves for each mode [14]. According to [15] et al and [16] et al, final failure separation on the damage zone is determined near nano-meter scale under the circumstances of investigating failure phenomenon near nano size crack or void by using tensile simulations.

1.3 Fracture Analysis Considering Uncertainty of Material Property

The wafer is designed in the form of a thin disk with a thin layered structure. While the diameter is on the millimeter scale, the thickness is a micro-scale structure, and each layered material is composed of a thickness of several nanometers. When designing a wafer structure, materials of each layer are sprayed to build a stacked structure. Since each layered material is too thin on the nanoscale, it is difficult to uniformly spray the surface of the material. As a result, wafer materials of each layer are built non-uniformly, so surface roughness or heterogeneity issues occur on the surface.

Due to this non-uniform material structure, the physical property values vary depending on the material surface location, and the interfacial properties between layers also have different values depending on the location. Therefore, it is important to resolve the uncertainty of wafer material properties and the interfacial properties of each material that occur at the nanoscale. In addition, the uncertainty of the material and interfacial properties greatly affects the structural fracture analysis of the wafer film. In particular, the degree of fracture and behavior of the wafer vary greatly depending on the size of the interfacial properties. Therefore, a fracture analysis that reflects the uncertainty of wafer material and interfacial properties should be performed. The uncertainty issue at the nanoscale is also an important issue in other materials or composites, and studies to solve this problem through simulation analysis are being conducted recently. Shin et al [17] introduced a probability distribution-based analysis to solve the uncertainty of particle size and young's modulus present in polymer nanocomposites, and presented uncertain properties based on statistics. A statistical-based polymer nanocomposite model was constructed using the material properties and particle size indicated on the basis of statistics. Vu-Bac et al [18] presented the distribution of chain length, temperature, and strain rate, which are uncertain factors present in the analysis of polyethylene polymer properties based on statistics. And the properties of polymer materials reflecting these probability distribution-based factors were analyzed through MD simulations. As such, the uncertainty of material properties observed at the nanoscale is reinterpreted based on probability distribution, and statistical-based interpretation

using this is emerging in recent studies.

In addition, in consideration of the uncertainty of material and composite properties, studies on statistical-based structural fracture analysis are being conducted recently. Gao et al [19] analyzed the fatigue failure of concrete materials based on statistics. Through this statistical-based fatigue fracture analysis, a model was built to predict the damage distribution according to the applied force. Lemos et al [20] calculated the polymer microstructural properties by Monte-Carlo simulations. Continuous segregated system of polymer microstructures were described by using stochastic technique.

1.4 Objectives and Contributions

The purpose of this study is to propose the multiscale wafer fracture model considering the uncertainty of material properties based statistical technique to describe fracture analysis of laminated wafer structure. To achieve the objective of the multiscale strategy, statistical MD simulations and continuum analysis are both carried out to construct the statistical fracture model of wafer film. In order to investigate the uncertainty of material properties and interfacial characteristics of wafer film, statistical MD models are proposed in this study. Those statistic-based uncertainty data sets are used to characterize the statistical fracture criterion, which describes the uncertainty of interfacial bonding conditions of wafer film. Thus, statistical wafer fracture model is proposed based those statistical material & interfacial characteristics considering uncertainty in nano-scale by using cohesive

zone model. Unlike the previous wafer fracture model, the proposed model can perform statistical-based fracture analysis and predict the yield rate of wafer structure. Unlike the existing fracture analysis, this statistical-based fracture analysis can predict how far the fracture has progressed and what will happen in the future, and can assume an error range of the degree of fracture. In addition, the yield of the wafer structure can determine which materials to use and construct, which is expected to increase the efficiency of the semiconductor process industry.

1.4 Thesis Outline

The aim of this dissertation is to organize the statistical wafer fracture model considering uncertainty of material & interfacial properties by multi-scale simulations. Herein, a systematic simulation methodology is suggested from the atomistic scale to continuum scale because the interfacial fracture phenomena of wafer film are indicated across a wide range of length scale. In order to analyze the uncertainty of material properties and interfacial characteristics of wafer film, statistical-based analysis method is introduced. To perform the simulation strategy, atomic models for wafer materials are constructed repeatedly in same structural conditions by MD simulations. Statistical thermos-mechanical properties such as young's modulus and coefficient of thermal expansion are derived by those models. Furthermore, traction-separation curves for normal and shear directions are obtained repeatedly by MD simulations. Statistical-based fracture properties such as fracture

toughness, fracture stiffness, and critical stress are calculated from those repeated MD traction-separation data sets, which is based on the normal distribution function. Statistical traction-separation curves are determined by those statistical properties for each fracture mode, which is also based on the normal distribution. The statistical fracture criterion is characterized by using those data set and mode mixity based power-law criterion, which is determined by Monte-Carlo simulations. Based on those statistical material properties and interfacial bonding conditions, fracture FEM model for wafer film is constructed by using cohesive zone model. In order to consider the probability distribution of material and interfacial properties together, the FEM model is constructed using Monte-Carlo simulations. To compared the proposed wafer model with conventional wafer fracture model, 3D plate model is suggested, which is conventionally used for wafer systematic model. The destruction of the wafer model that occurs when the temperature is raised from 0K to 800K is analyzed. This is because the interfacial thermal stress is dominantly applied at the interface of the structure due to the difference in CTE between each material. It is seen that the proposed model investigate the interfacial fracture behavior much better than the previous wafer fracture model. In addition, unlike the conventional model, the proposed model present the yield rate of wafer structure according to heating temperature.

The detailed simulation statistical multiscale framework is addressed in this study that is characterized as follows. Chapter 2 focuses on constructing the statistical wafer fracture model by MD simulations. Based on statistical material and

interfacial properties of wafer film, statistical mixed-mode fracture criterion is characterized by Monte-Carlo simulations. Furthermore, statistical wafer fracture model is constructed by using cohesive zone model by multi-scale simulations. The fracture model considers statistical material and interfacial properties together, which is characterized by Monte-Carlo simulations. Chapter 3 provide the applications of statistical wafer fracture model. 3D plate model is considered to simulate the wafer fracture behaviors under thermal heating process from 0K to 800K. By using the wafer model, the proposed model is compared with conventional wafer fracture model, which provide degree of failure and yield rate of wafer system. Chapter 4 summarizes conclusions of this study and outlines of future tasks.

Chapter 2

Wafer Fracture Model Considering Uncertainty

2.1 MD Model Considering Uncertainty

The wafer is constructed in the form of a laminated stacked structure, which is a nano-scale structure with a very thin thickness. As a result, it is constructed with non-uniform material layers, and material properties or interfacial properties vary depending on the location. In order to resolve these uncertainties in material and interface properties, a statistical-based property analysis technique is introduced in this study. Before performing statistical-based analysis techniques, we consider the molecular model of SOH polymer and silicon nitride (SiN) material by using

Material studio 5.5 (Accelrys Inc.), which is depicted in Fig. 2.1 (a) and (b). For the specification of the bond and interatomic non-bond interactions, PCFF force field is used in those models. After constructing all-atom models of those corresponding materials, the unit cells are equilibrated by followed relaxation simulations as an energy minimization, NVT ensemble, and NPT ensemble under the conditions of 300K and 1 atm. In order to check the consistency of these equilibrated molecular cells, thermo-mechanical properties such as young's modulus and the coefficient of thermal expansion (CTE) are calculated and compared with experimental values, which are listed in table 2.1. It is showed that those thermo-mechanical properties of atomic models fit well with the experimental values, which shows that consistency of those molecular models [21, 22, 23, 24].

In order to use statistic-based technique, the thermo-mechanical properties of each cell are calculated after repeatedly generating all-atom cells for SOH polymer and SiN under the corresponding structural conditions. Each of those cells has the same simulation conditions but exhibits slightly different physical quantities due to inherent uncertainties, and thus the corresponding calculated thermo-mechanical properties have different values. Those physical quantities show in the form of probability distributions, which is described in Fig. 2.2. Fig. 2.2 represent the normal distribution of modulus and CTE for SOH and SiN. Those distributions of properties are tabulated in Table 2.2. Through those distributions of physical quantities, material characteristics reflecting uncertainties of SOH polymer and SiN can be presented on a statistical basis.

2.2 Traction-Separation Curves for Fracture Modes

In order to investigate the fracture analysis on the interface of laminated composite structure, the traction-separation model is considered to characterize the interfacial fracture properties by molecular dynamics simulations. In this study, the traction-separation model of SiN/SOH was constructed in the form of bi-layer model by combining above validated unit cells in this study, which is depicted in Fig. 2.3. The bi-layer model was performed by fracture tensile simulations for normal mode and shear mode to by using the Large-Scale Atomic/Molecular Massively Parallel Simulator (LAMPPS, Sandia Lab) to identify traction-separation curves for each fracture mode at the interface of wafer film, which is depicted in Fig. 2.4. Fig. 2.4 illustrate the schematic diagram of fracture tensile simulations for normal mode and shear mode and the blue zone represent the interface slab of the model. During those tensile simulations, a traction stress at atomic scale of designated atoms is calculated according to separation distance in the blue zone for each fracture mode as described by the virial theorem. In order to reflect the uncertainties of these interfacial fracture properties, T-S curves for each fracture mode are calculated through repeated MD simulations as in the previous case for thermo-mechanical properties of SOH and SiN. Iterative simulations are performed while gradually increasing the number of T-S data sets, which are shown in Fig. 2.5 and Fig. 2.6. Fig. 2.5 show T-S data sets for normal mode with different number of data sets of 3450, 9440, and 17250. T-S data sets for shear mode with different number of data points of 3450, 9440, and

17250 are depicted in Fig. 2.6. In order to observe how the distribution of T-S data sets change as the number of data points increases, the probability distribution of critical stress (T), fracture stiffness (K), and fracture toughness (G) are calculated from the T-S data points for each case, respectively. Those fracture properties also appear in the form of a normal distribution function, and the standard deviation (S.D) values for each property distribution are calculated and compared according to the number of data points, which are shown in Fig. 2.7. Fig. 2.7 describe the standard deviation of T, K, and G for normal mode according to number of T-S data points. In those graphs, it is seen that standard deviation values converges as the number of data points increase. Therefore, statistical data analysis is performed with 17250 T-S data points for normal mode and shear mode, which is depicted in Fig. 2.8 (a) and (b). The traction stresses are distributed for each mode, which is especially more distributed in damage evolution region than damage initiation region. This result shows that the uncertainty increases when failure occurs in the plastic region that in the elastic region.

Fracture properties of critical stress, fracture stiffness, and fracture toughness are calculated from those 17250 T-S data sets, which are depicted in Fig. 2.9 and Fig. 2.10. Fig. 2.9 represent the normal distribution of T, K, and G for normal mode and Fig. 2.10 show that for shear mode. In order to check the consistency of those distributions of fracture properties for each mode obtained in Fig. 2.9 and Fig. 2.10, those standard deviation values are compared with experimental based reference data, which are tabulated in Table. 2.3 [25-30]. In order to find out the correlation between

those variables, the correlation and covariance for T, K, and G for each mode are analyzed as shown in Fig. 2.11 and Fig. 2.12. Fig. 2.11 represent the correlation and covariance (ρ) for G-T, T-K, and K-G for normal mode, also Fig. 2.12 show that for shear mode. It is seen that the correlation of each variable is close to linear, also the covariance for each variable is close to 1 for each mode. The result means that the corresponding variables according to each mode show a dependent relationship. Therefore, the distributed T-S data points in Fig. 2.8 (a) and (b) can be statistically represented as Fig. 2.13 (a) and (b). During such statistic data processing, the bi-linear fitting is performed together. Fig. 2.13 (a) show the statistic T-S curve based on the normal distribution for normal mode, and Fig. 2.13 (b) describe that for shear mode. Therefore, through this statistical data processing, statistical-based T-S diagrams according to each failure mode can be derived and interfacial fracture properties can be presented on a statistical basis for each mode.

2.3 Statistical Mixed-Mode Fracture Criterion

In the previous section, statistical T-S curves for each mode are derived considering the uncertainties of interfacial bonding conditions on the interface of wafer film. The statistical-based T-S curves are investigated to calculate statistical fracture properties for each mode, which is described as:

$$G_N = G_{N\,avg} + \sigma_{G_N} \text{Rand}_N \quad (1)$$

$$T_N = T_{N\,avg} + \sigma_{T_N} \text{Rand}_N \quad (2)$$

$$K_N = K_{N\text{avg}} + \sigma_{K_N} \text{Rand}_N \quad (3)$$

$$G_S = G_{S\text{avg}} + \sigma_{G_S} \text{Rand}_S \quad (4)$$

$$T_S = T_{S\text{avg}} + \sigma_{T_S} \text{Rand}_S \quad (5)$$

$$K_S = K_{S\text{avg}} + \sigma_{K_S} \text{Rand}_S \quad (6)$$

Where G_N, T_N, K_N are statistical-based fracture toughness, critical stress, and fracture toughness for normal mode and G_S, T_S, K_S are that for shear mode. Also, $G_{N\text{avg}}, T_{N\text{avg}}, K_{N\text{avg}}$ are average value of each properties for normal mode, and $G_{S\text{avg}}, T_{S\text{avg}}, K_{S\text{avg}}$ are that for shear mode. $\sigma_{G_N}, \sigma_{T_N}, \sigma_{K_N}$ are standard deviation of each parameters for normal mode, and $\sigma_{G_S}, \sigma_{T_S}, \sigma_{K_S}$ are that for shear mode. The statistical fracture properties are defined by the mean value and their standard deviation, so their statistical value is determined depending on random number as in Eq. (1), (2), (3), (4), (5), and (6) for each mode. Since those parameters are dependent relationship for each mode, the same random number is given according to mode. Thus, random numbers for normal mode are described as Rand_N and that for shear mode are Rand_S .

Accordingly, statistical fracture properties based on the normal distribution for each fracture mode are calculated as shown in Eq. (1), (2), (3), (4), (5), and (6). Statistical fracture criterion is newly proposed by inserting the above obtained properties into the mixed-mode fracture criterion by using mode mixity of the wafer film. The SOH/SiN wafer model is constructed in Appendix A, and the interfacial fracture properties in normal mode, shear mode, and mixed mode are calculated. Also the methodology of constructing the mixed-mode fracture criterion based on

the power-law criterion are described by using those fracture properties and the process of calculating the mode-mixity of the wafer composite material is described. The whole schematic diagram for characterization of statistical fracture criterion is described in Fig. 2.14. The mode-mixity of the wafer composite material calculated in Appendix A is fixed, and the previously obtained parameters are input differently into criterion according to $Rand_N$ and $Rand_S$. Since the parameters for normal mode and shear mode are independent variables from each other, $Rand_N$ and $Rand_S$ are also independent relationship with each other. Therefore, each parameter can be inserted into criterion at random, and Monte-Carlo simulation is used to interpret it based on statics in this study. In this study, it is performed 10^3 times, and as a result, the fracture criterion based on the normal distribution is determined as shown in Fig. 2.15. Fig. 2.15 represent that the blue line is the average value diagram, and red and green lines are the diagrams of $\pm 2\sigma$ values, respectively. Moreover, statistical mixed-mode cohesive law is characterized based on the criterion as shown in Fig. 2.16. Fig. 2.16 illustrate the T-S curves for each mode and their criterion. The statistical fracture criterion provide mixed-mode fracture properties for loading angle from 0 degree to 90 degree as a normal distribution curve. Thus, interfacial failure characteristics of wafer film for each loading angle are calculated as an average value and confidence range from the curve.

2.4 Wafer Fracture Model by Multi-Scale Simulations

In previous sections, it is investigated that statistical thermo-mechanical properties of SOH polymer and SiN considering uncertainties of material properties. Furthermore, statistical T-S curves are derived by bi-layer model for normal mode and shear mode, which provide statistical fracture properties for each mode. By using Monte-Carlo simulations, statistical fracture criterion on the interface of the wafer film is characterized considering uncertainties of interfacial bonding conditions of laminated wafer structure. It is intended to predict the fracture behaviors of laminated wafer structure considering those statistical material and interfacial properties by multi-scale simulations in this Chapter.

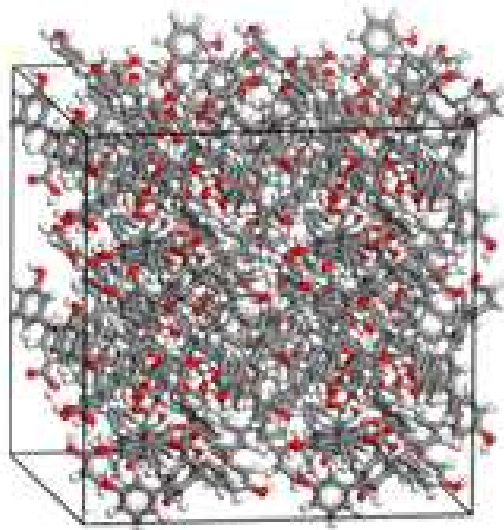
Among the FEM analysis models that simulate the fracture behavior of composite materials, cohesive zone model has been used in many researches. Moreover, the cohesive zone model is used for investigate the fracture analysis of the wafer film in recent studies. The cohesive zone model for laminated wafer structure is designed to the three-phase model consisting of each material and the interface. In particular, the interface region is a dominant phase of the model because the main failure mechanism of the wafer film is evaluated in that area. The cohesive zone elements are defined to properly express the interfacial bonding conditions in laminated wafer structure, which is determined by cohesive parameters such as fracture toughness, fracture stiffness, critical traction stress, and mode mixity. Thus, it is an important issue in constructing the cohesive zone model that defining the

effective thickness of cohesive zone elements, which is addressed with in more detail in Appendix B.

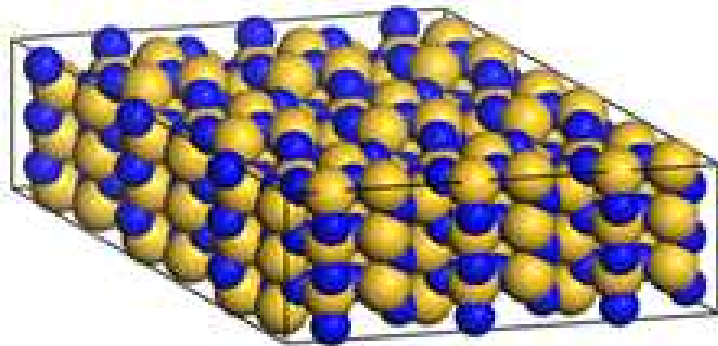
In order to characterize the statistical wafer fracture model of laminated wafer structure, statistical multiscale bridging method is proposed, which is substituting the numerical analysis values at the nano scale into the continuum scale model based statistical technique. The bridging methodology is divided into two steps that are inserting material and interface parameters, and determining statistical FEM results, which are illustrated in Fig. 2.17 and Fig. 2.18. Fig. 2.17 show the schematic flow for step 1 of constructing the wafer fracture model. In first step, statistical material and interface properties are inserted in to the finite element model of the wafer system as in the form of a normal distribution function. Those material properties are elastic modulus and CTE of SOH polymer and SiN and those interface properties are critical stress, fracture stiffness, and fracture toughness for mixed-mode state, which are calculated in Chapter 2 by MD simulations. Those statistical material and interface parameters have different normal distribution function, resulting in different cohesive zone model according to random number.

Fig. 2.18 describe the schematic flow for step 2 of constructing the wafer fracture model. In step 2, In order to obtain the finite element analysis of the fracture model composed of those properties representing different probability distributions, the model would be constructed as a function based on one probability distribution. Thus, Monte-Carlo simulations are performed to determine the wafer fracture model as a one normal distribution function. 10^3 trial of Monte-Carlo simulations are

addressed in this study, so the wafer fracture model reflect the uncertainties of material and interface characteristics together. Statistical FEM analysis based on normal distribution function is determined by above process from the wafer fracture model. It is possible to design a wafer fracture model in various shaped and external conditions reflecting the uncertainties of the wafer composite material with the proposed model. In addition, the fracture analysis results based on probability distribution can be presented through the proposed model, which provides different numerical analysis from the existing wafer fracture model.



(a) SOH polymer



(b) SiN

Figure 2.1 All-atom model of (a) SOH polymer and (b) SiN.

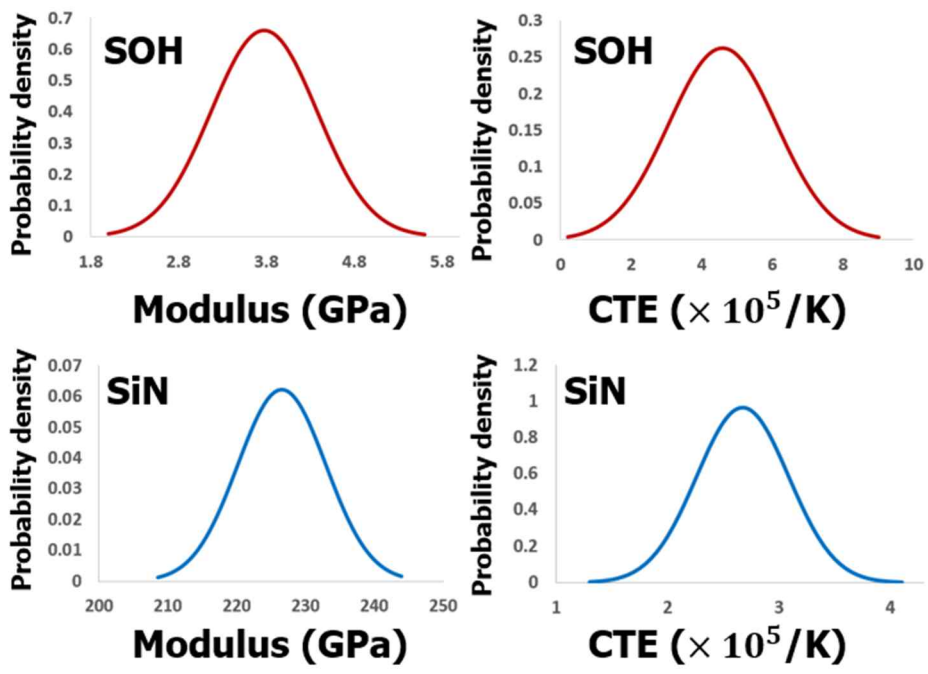


Figure 2.2 Probability distribution of modulus and CTE.

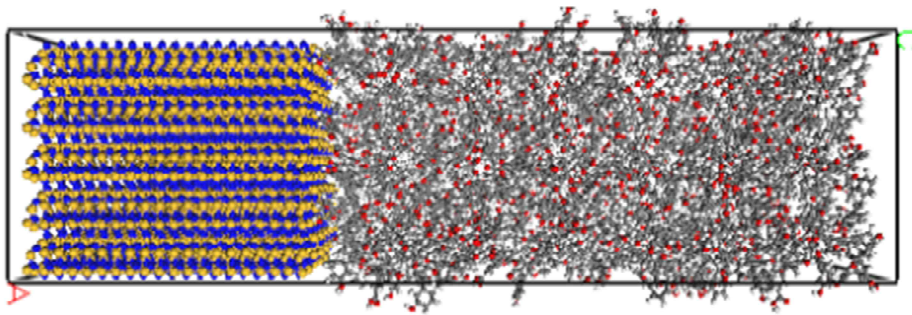


Figure 2.3 Bi-layer model of SiN/SOH traction–separation model.

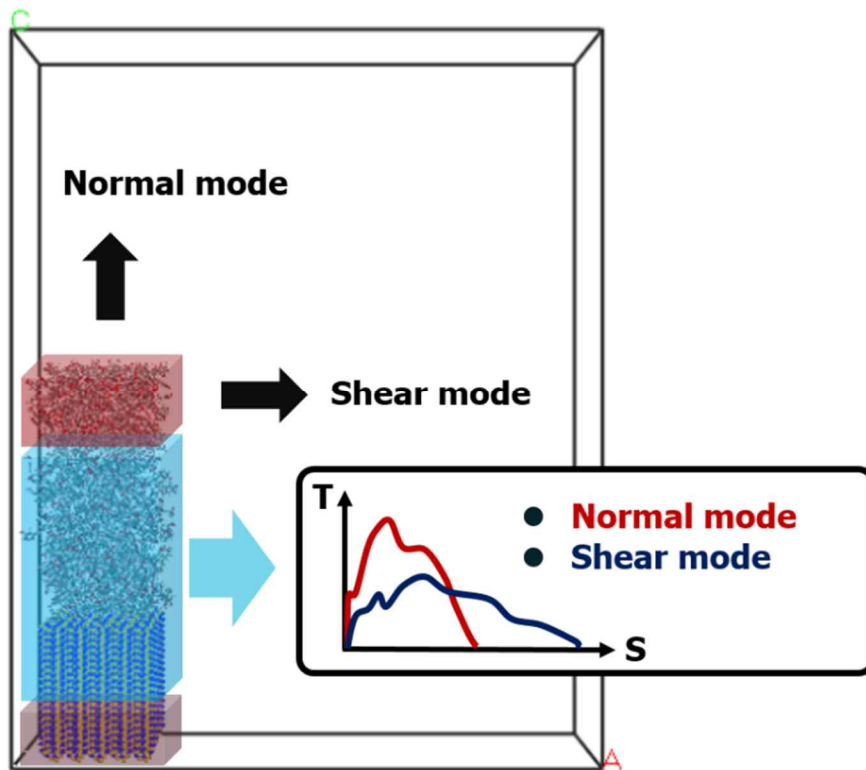


Figure 2.4 Schematic diagram of fracture simulations.

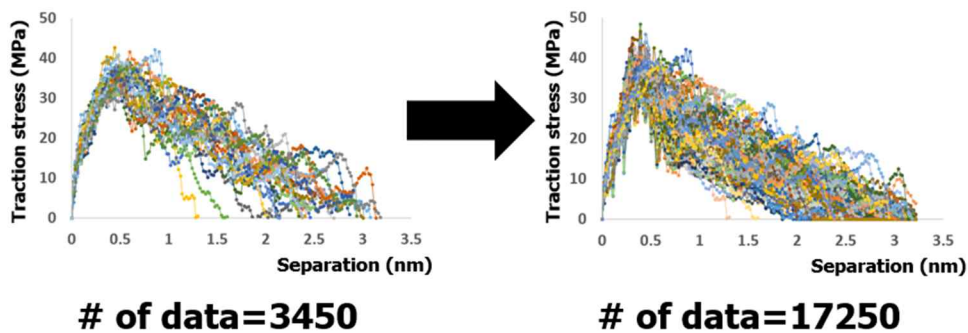


Figure 2.5 T-S data for normal mode with different number of data sets.

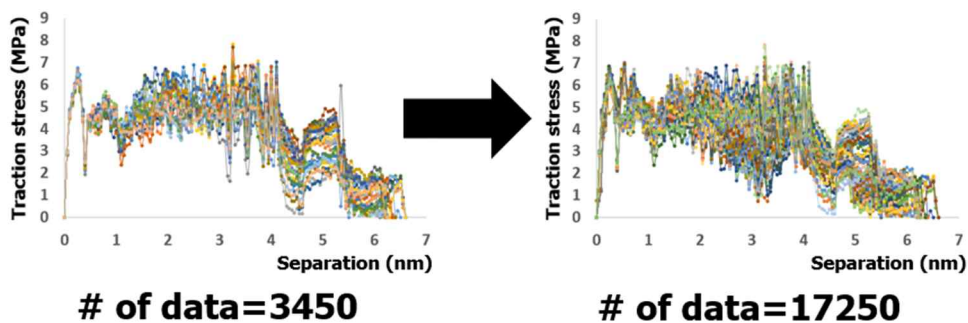


Figure 2.6 T-S data for shear mode with different number of data sets.

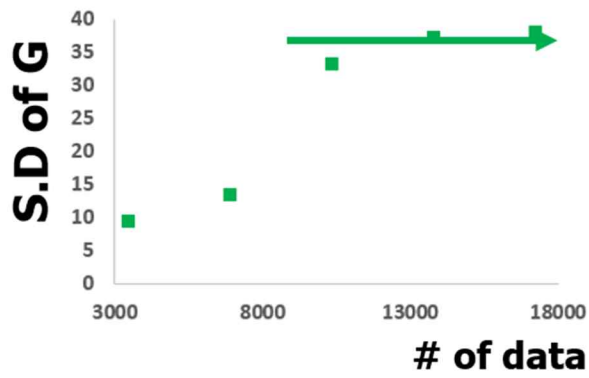
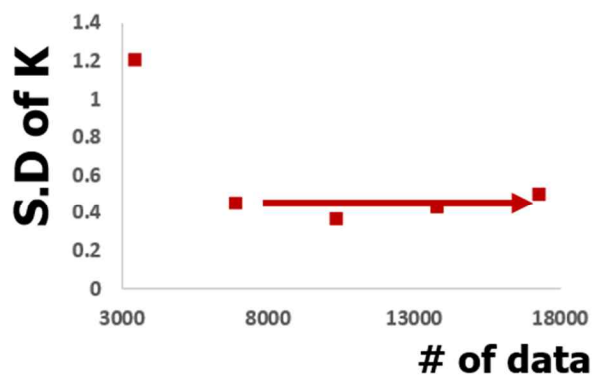
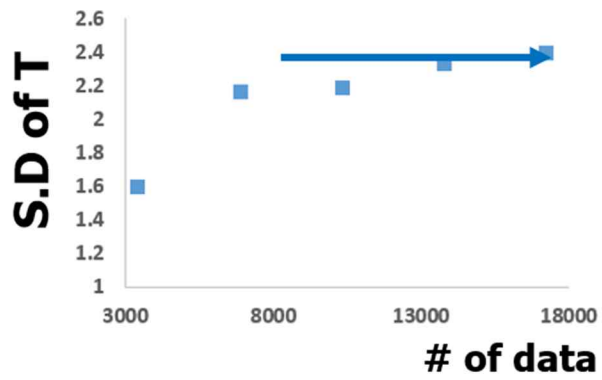
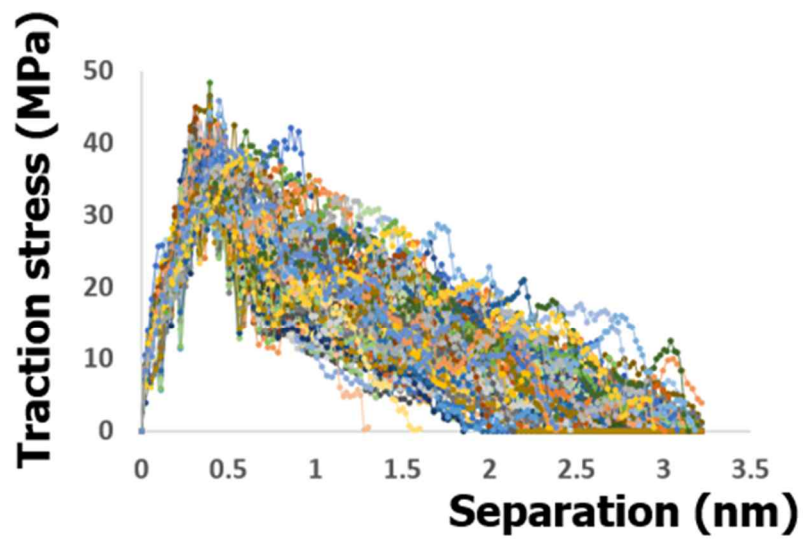
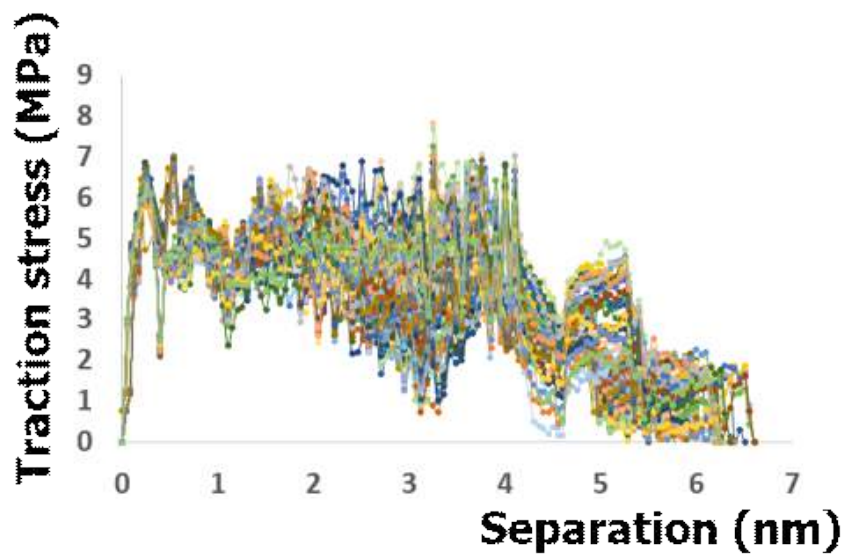


Figure 2.7 Standard deviation of T, K, and G for normal mode according to # of data points.



(a) T-S data sets for normal mode



(b) T-S data sets for shear mode

Figure 2.8 T-S data sets for (a) normal mode and (b) shear mode by MD simulations.

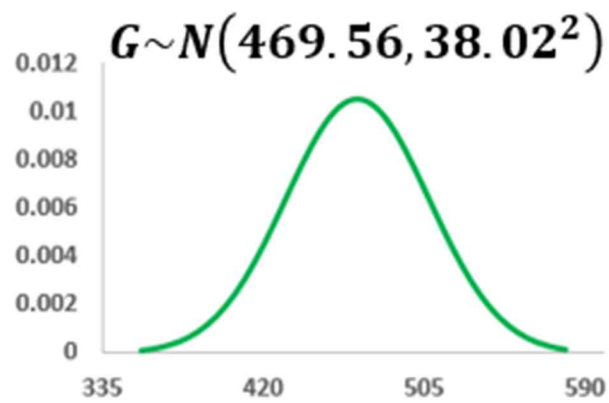
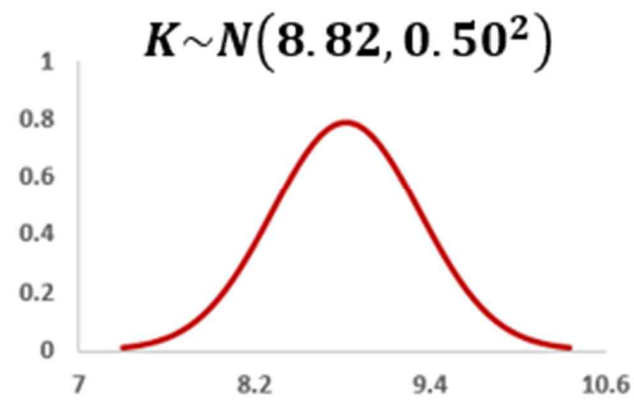
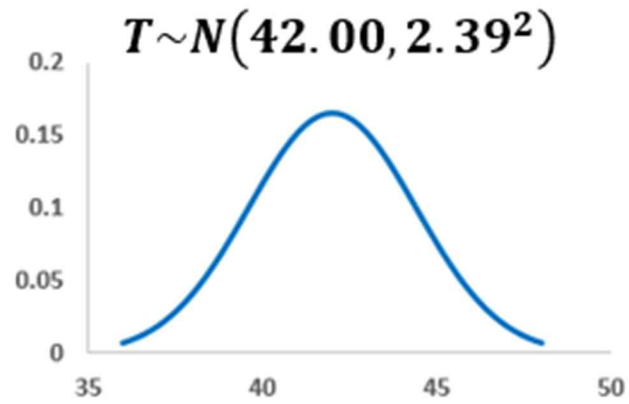


Figure 2.9 Normal distribution curves for normal mode.

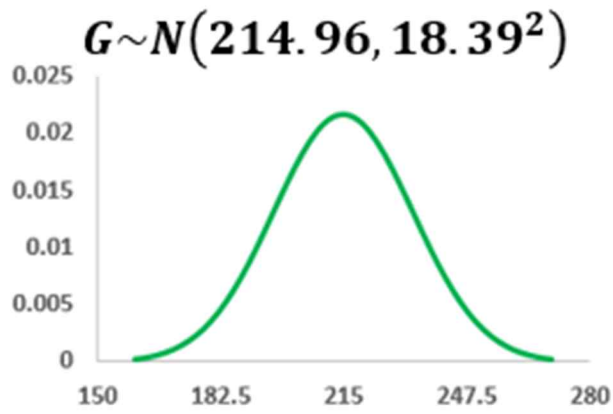
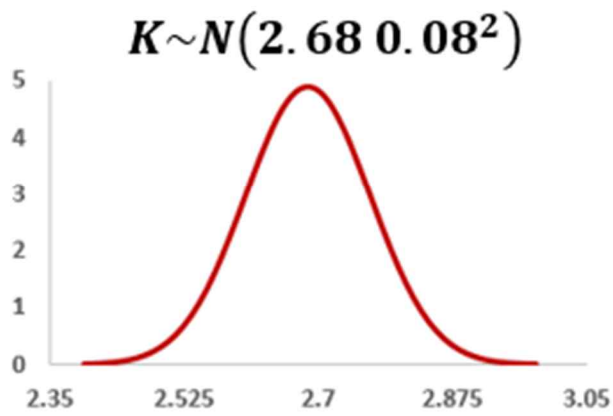
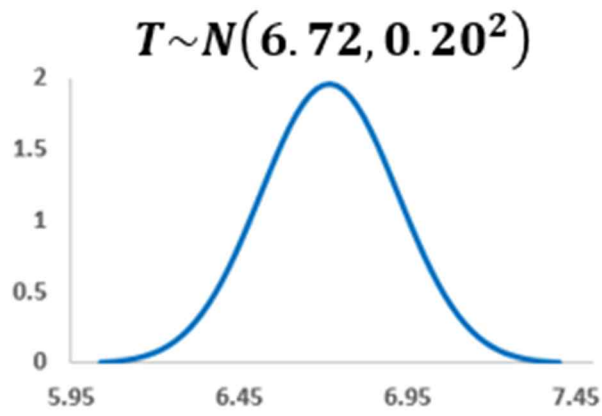


Figure 2.10 Normal distribution curves for shear mode.

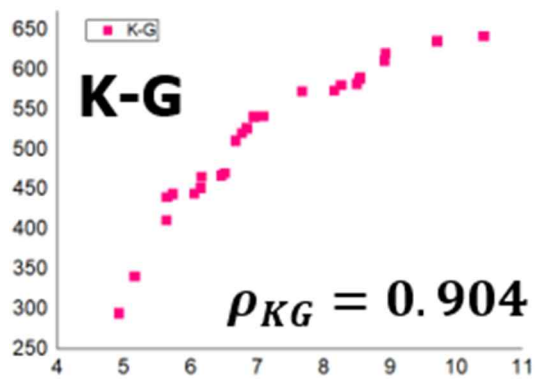
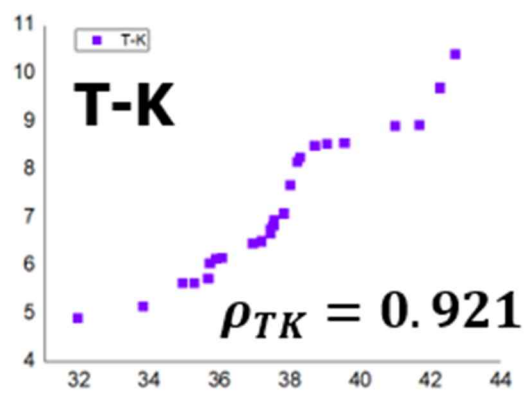
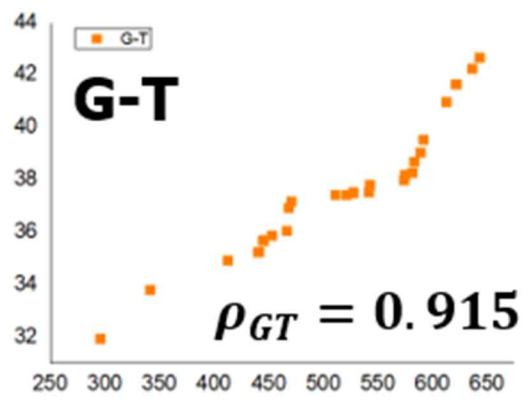


Figure 2.11 Correlation between T, K, G for normal mode.

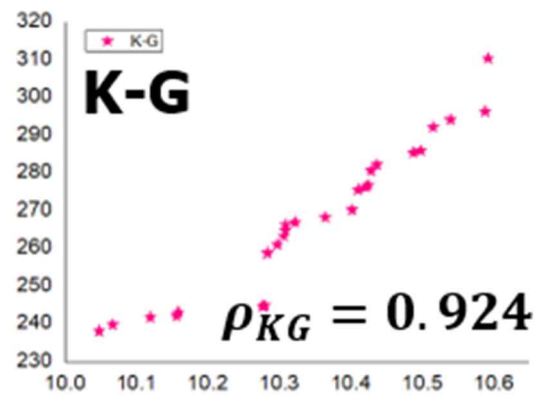
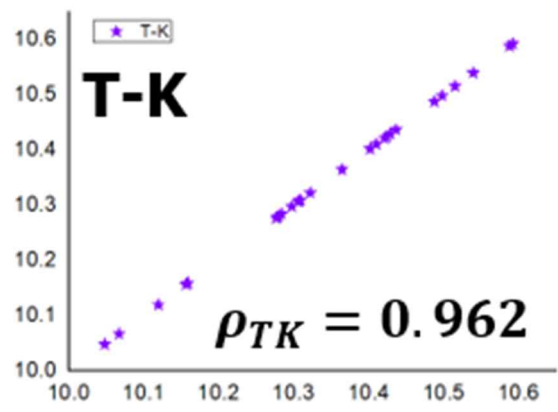
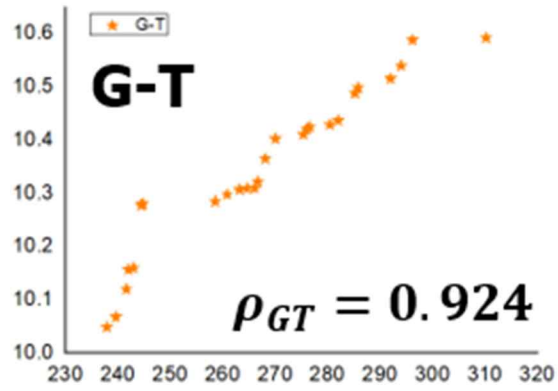
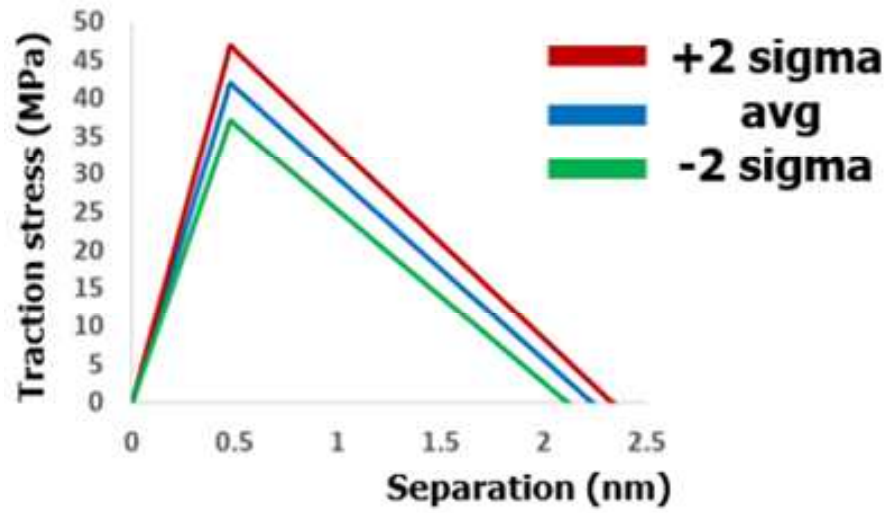
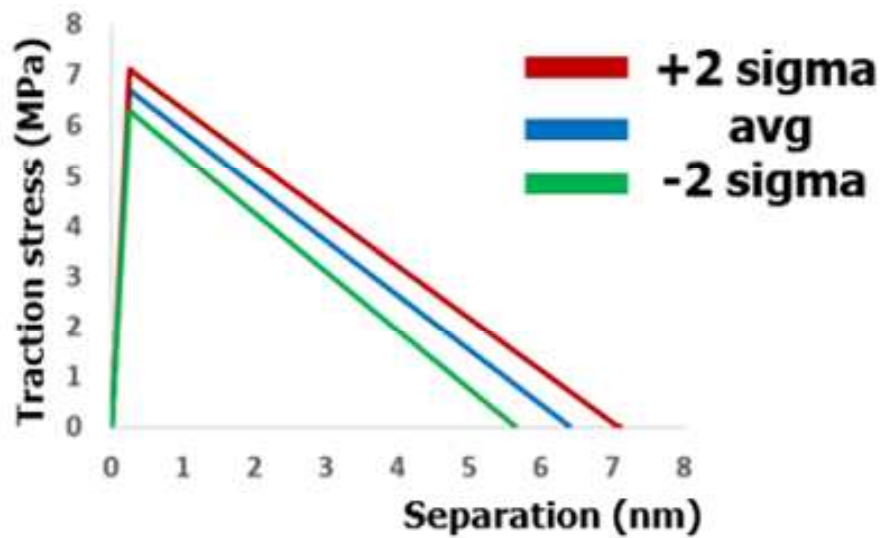


Figure 2.12 Correlation between T, K, G for shear mode.



(a) Statistical Normal T-S curve



(b) Statistical Shear T-S curve

Figure 2.13 Statistical T-S curves for (a) normal mode and (b) shear mode by MD simulations.

Statistical properties



Normal mode
 $G_{N_{avg}} + \sigma_{G_N} Rand_N$
 $T_{N_{avg}} + \sigma_{T_N} Rand_N$
 $K_{N_{avg}} + \sigma_{K_N} Rand_N$

Shear mode
 $G_{S_{avg}} + \sigma_{G_S} Rand_S$
 $T_{S_{avg}} + \sigma_{T_S} Rand_S$
 $K_{S_{avg}} + \sigma_{K_S} Rand_S$



Mixed-mode fracture criterion

- ✓ Quadratic stress criterion
- ✓ Power law criterion
- ✓ Mode-mixity (α): 0.552
- ✓ **Monte-Carlo simulation**



Statistical fracture criterion



Mixed mode
 $G_m = G_{m_{avg}} + \sigma_{G_m} Rand$
 $T_m = T_{m_{avg}} + \sigma_{T_m} Rand$
 $K_m = K_{m_{avg}} + \sigma_{K_m} Rand$

Figure 2.14 Schematic flow for statistical fracture criterion.

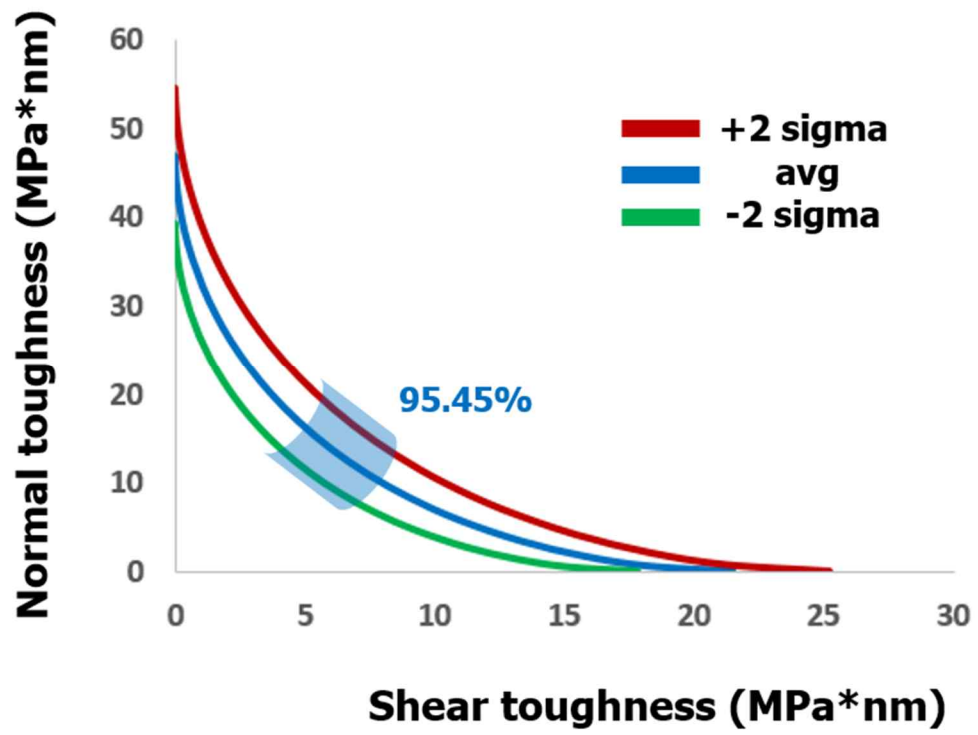


Figure 2.15 Statistical fracture criterion based on normal distribution.

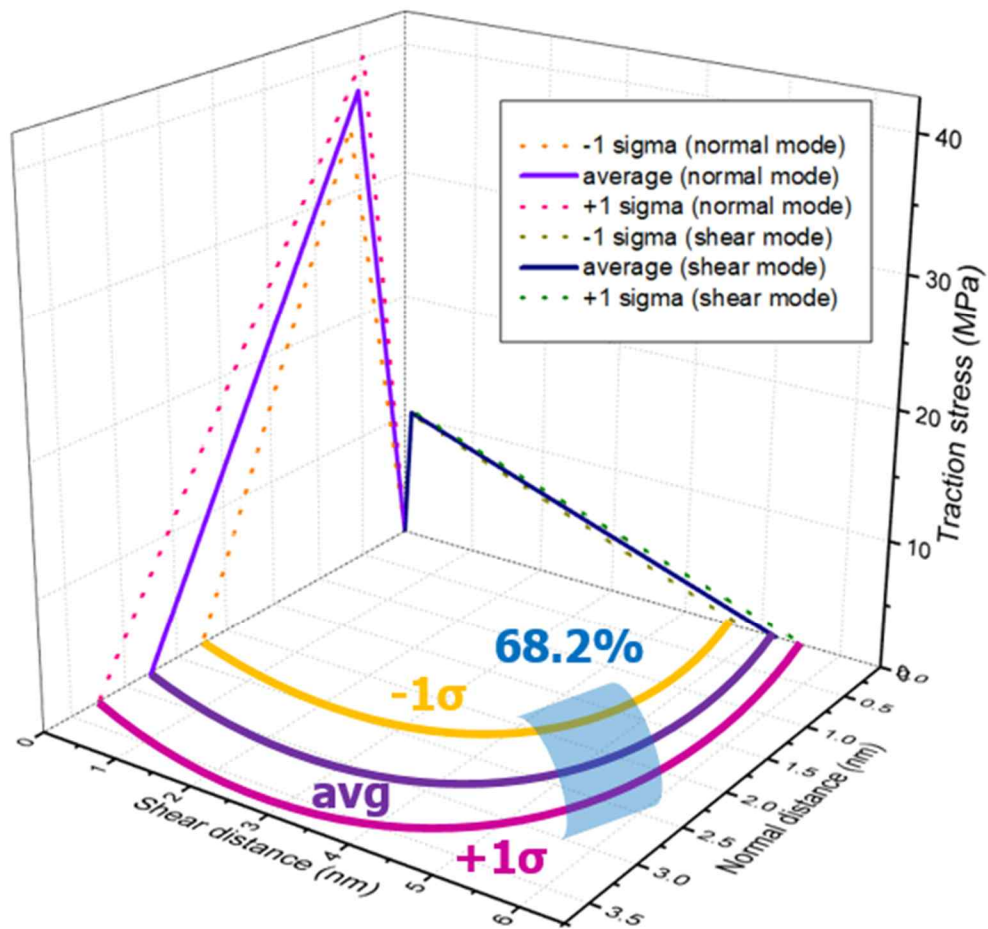


Figure 2.16 Statistical mixed-mode cohesive law based on normal distribution.

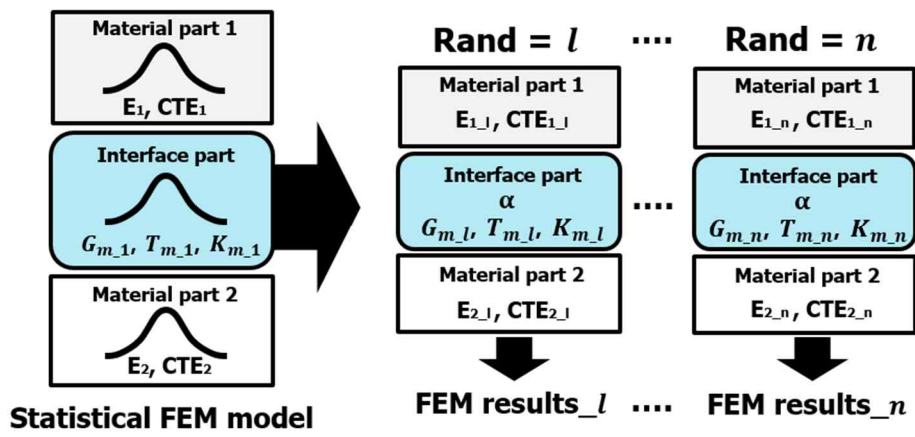


Figure 2.17 Schematic flow for step 1 of constructing the wafer fracture model.

FEM results_1 FEM results_l FEM results_n



Monte-Carlo simulation (n trial)

Statistical FEM solutions

$$FEM\ results_m = FEM\ results_{m_avg} + \sigma_{FEM\ results_m} Rand$$

Figure 2.18 Schematic flow for step 2 of constructing the wafer fracture model.

Table 2.1 Thermo-mechanical properties of SOH and SiN.

| Material | Young's modulus (GPa) | | CTE (/K) | |
|----------|-----------------------|--------------------|-----------|-----------------------------|
| | MD value | Experimental value | MD value | Experimental value |
| SOH | 3.77 | 4.00 [16] | 45.80E-06 | 59.00E-06 [17] |
| SiN | 226.50 | 235.00 [18] | 2.60E-06 | 2.00E-06 ~ 4.00E-06 [19] |

Table 2.2 Normal distributions of thermos-mechanical properties for SOH and SiN.

| Material | Young's modulus (GPa) | CTE (/K) |
|----------|---------------------------|----------------------------|
| SOH | $E \sim N(3.77, 0.60^2)$ | $CTE \sim N(4.58, 1.52^2)$ |
| SiN | $E \sim N(226.5, 6.41^2)$ | $CTE \sim N(0.26, 0.41^2)$ |

Table 2.3 Standard deviation of T, K, and G for each mode compared with reference data.

| | S.D for normal mode | | S.D for shear mode | |
|----------|---------------------|--|--------------------|------------------------------------|
| | MD data | Ref. | MD data | Ref. |
| S.D of T | 2.39 | | 0.20 | 0.25 [25], 0.35 [26] |
| S.D of K | 0.50 | | 0.08 | |
| S.D of G | 38.02 | 27.80, 30.90 [27], 34.80 [28], 28.50 [29] | 18.39 | 12.80, 14.51 [27], 11.4 [30] |

Chapter 3

Applications of Statistical Wafer Fracture Model

3.1 Statistical Multi-Scale Modeling for Wafer Film

Finite element models of various shapes have been constructed to investigate the fracture analysis for wafer film under external environments. Among them, in particular, a laminated plate model that mimics the layered structure of a wafer film has been mainly used in many researches. In particular, using the plate model, it is easy to observe the interfacial failure between wafer materials caused by external forces, and it is appropriate to understand the fracture mechanism. 3D plate model is suggested to identify the fracture behavior of laminated wafer structure in this study,

which is depicted in Fig. 3.1. The system size reflects the length of laminated wafer structure actually used, and a void area is formed in the center of the wafer film.

The laminated wafer structure is destroyed by various factors, such as pressure, oxidation process, laser radiation, and thermal stress. However, such a manufacturing process of wafer film has a very large temperature difference from 0K to 600K or 800K. The wafer system has a multi-layered structure since each material has a different CTE, which reacts sensitively to such a large temperature change. Due to the difference in CTE of each material layer, a large interfacial thermal stress is applied on the interface region, which results in frequently destroyed wafer structure during manufacturing process. Therefore, in this study, the destruction of laminated wafer structure caused by thermal stress was intensively analyzed. Also it is observed that it deforms as shown in Fig. 3.2 when thermal stress is applied to the proposed plate model. Fig. 3.2 (a) show the undeformed state of the 3D plate model under 0K and Fig. 3.2 (b) represent the deformed state of the model under 800K. The interfacial thermal stress is applied at the interface region of the wafer film due to the difference in CTE between SOH polymer and SiN when the thermal stress is applied. Accordingly, the crack propagation appears starting from the void region according to temperature rise.

3.2 Comparison Proposed Model with Conventional Model

In this study, in order to compare the newly proposed wafer fracture model and the existing wafer fracture models, the thermal stress is applied to the 3D plate model from 0K to 600K, 700K, and 800K to investigate the change in fracture behavior of the wafer film. The numerical analysis are compared with the perfect bonding model and cohesive zone model based simple power-law criterion introduced earlier in the introduction chapter, and those models are shown in Fig. 3.2. Fig. 3.2 (a) show the undeformed state of 3D plate model under 0K. Fig. 3.2 (b), (c), and (d) depict the deformed state of the model in the case of perfect bonding model, cohesive zone model based simple power-law criterion, and statistical fracture model.

In the case of the perfect bonding model, it is difficult to observe the fracture behavior at the interface because the model assumes the interfacial bonding condition to be perfect bonding. As a results, the overall structural shape also deforms differently depending on the temperature compared with other models. In the case of the cohesive zone model based simple power-law criterion, the expected fracture behavior is shown, respectively. Since the interface bonding characteristics are simply considered, we would like to observe the difference through numerical analysis and comparison. Lastly, in the case of statistical fracture model, structural deformation appears based on a normal distribution, and changes in physical properties due to the destruction also appear. The structural deformation of each model is compared by increasing the temperature sequentially from 0K to 600K,

700K, and 800K, which is tabulated in Table 3.1. As explained earlier, the degree of deformation is completely different from other models in the case of perfect bonding model, which does not reflect interfacial failure. In the case of cohesive zone model based simple power-law criterion, it is similar to the average value of statistical fracture model, but there is a slight difference because the interface bonding conditions is simplified assumed. The deformation values in the form of a normal distribution can be obtained when analyzed with the proposed statistical model, which provides the average deformation with their error range.

The fracture phenomenon for wafer film is observed when thermal stress is applied to the FEM model, and the SDEG distribution is employed to interpret it, which is shown in Fig. 3.4. Fig. 3.4 (a) illustrate the undeformed state of SDEG distribution and Fig. 3.4 (b) show the deformed state of SDEG distribution. In Fig. 3.4 (b), the destruction progresses from the void to the sides, and the destroyed area appears in red region, The SDEG distribution at the interface is calculated for each model, which is tabulated in Table 3.2. In the case of perfect bonding model, the SDEG distribution cannot be obtained because the interfacial failure does not occur in the model. In the case of cohesive zone model based simple power-law criterion, SDEG distribution is given as a single numerical value, whereas when a statistical model is used, it appears in the form a normal distribution function. The SDEG distributions of the cohesive zone model and statistical fracture model are depicted in Fig. 3.5. The red line is SDEG distribution for 600K, and the blue line is that for 700K, and the purple line is that for 800K in Fig. 3.5. It is seen that the SDEG mean

values are slightly different between those models, and in the case of a statistical fracture model, since it is given as a distribution, an error range can also be provided according to temperature. In the SDEG distribution obtained above, when the SDEG is 1, it is considered to be completely destroyed, and through this, the yield rate of each wafer model can be predicted, which is tabulated in Table 3.3. In the case of the perfect bonding model the yield rate of the system is 100% regardless of temperature since the interfacial failure does not occur. In the case of the cohesive zone model, the SDEG increases with temperature and the destruction progresses more, but since the value does not reach 1, it cannot be considered that the complete failure has occurred. Therefore, even in the case of the model, the yield rate is calculated as 100% regardless of the temperature. In the case of the statistical fracture model, since the SDEG distribution is defined as a normal distribution, the probability that the SDEG is 1 for each temperature can be predicted and the yield rate of the wafer model can be predicted according to the temperature. Through the model, it can be seen that the yield rate decreases rapidly as the temperature rises. Therefore, the yield rate of the laminated wafer structure according to the temperature when the structure is subjected to thermal stress through the proposed model can be presented.

To check how accurate the proposed wafer fracture model is compared to the existing wafer fracture model, comparison with experimental-based reference data was performed [31]. The schematic wafer model and experimental data specified in the reference are shown in Figure 3.6. Fig. 3.6 (a) show the wafer substrate model of polymer-SiN and Fig. 3.6 (b) represent the normalized debond length data according

to temperature. The fracture analysis is performed using the conventional wafer fracture model such as perfect bonding model and cohesive zone model based simple power-law criterion and statistical wafer fracture model, and the experimental values are compared, which is tabulated in Table 3.4. The trend is compared to how much the debond length changed as the temperature increased. As a result of the comparison, it is confirmed that the statistical fracture model show the most similar change trend. The statistical-based wafer fracture model proposed in this study is more accurate than conventional wafer fracture analysis models, and through statistical analysis, the error range and structural yield rate of fracture analysis can be newly presented.

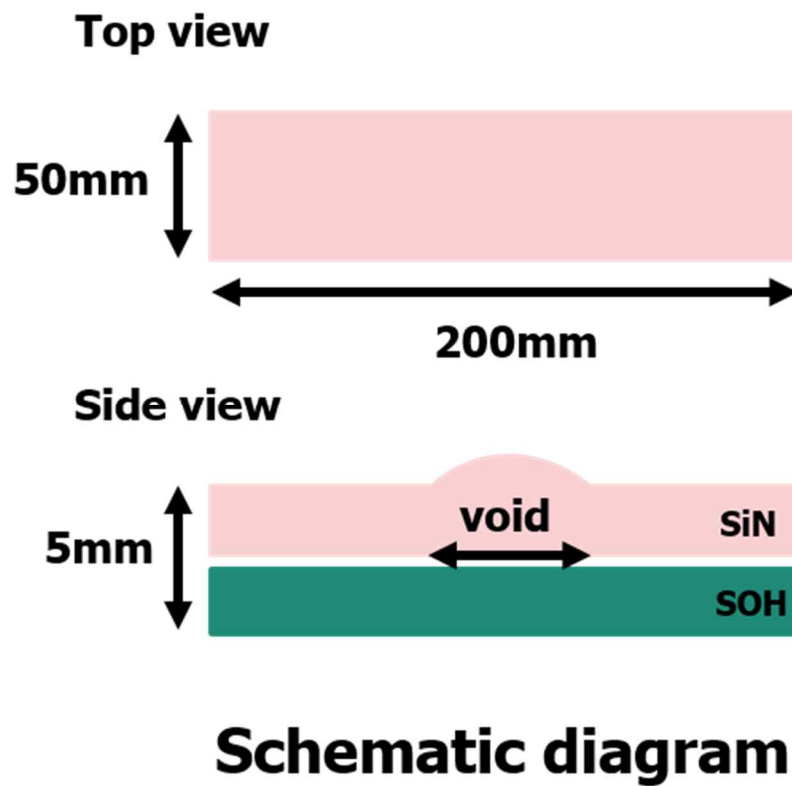
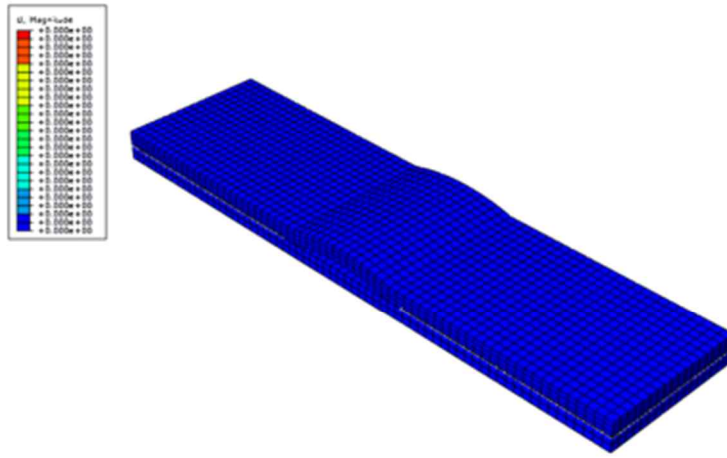
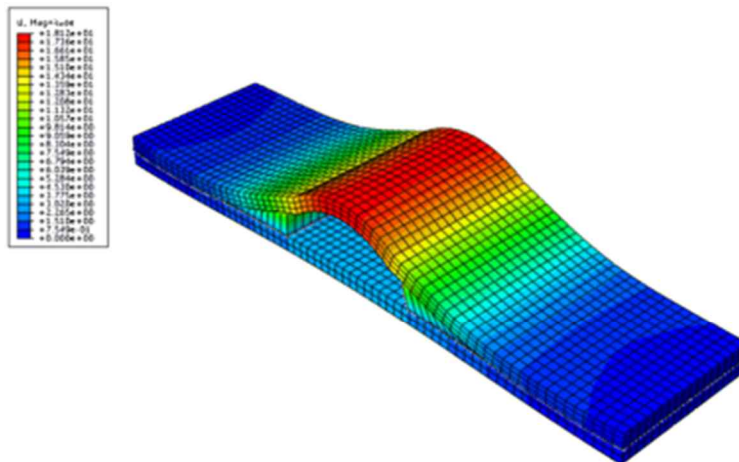


Figure 3.1 Schematic diagram of 3D plate model.



(a) Undeformed state



(b) Deformed state

Figure 3.2 3D plate model of (a) undeformed state and (b) deformed state from 0K to 800K.

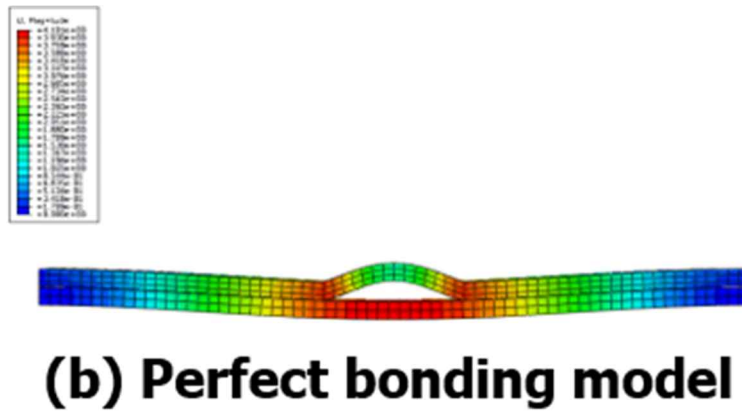
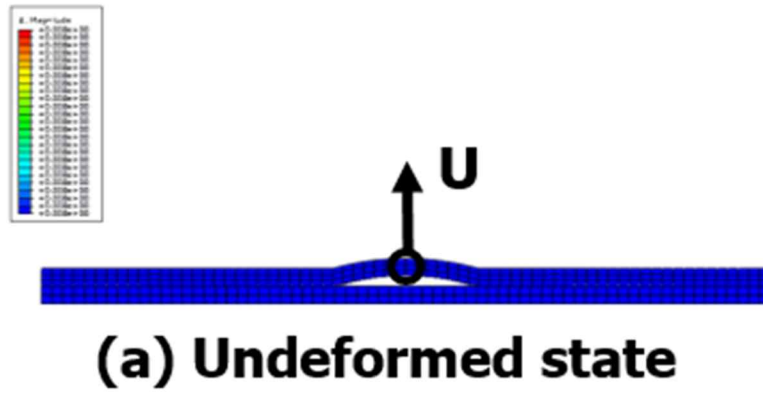
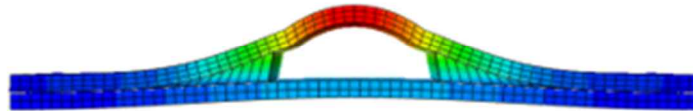
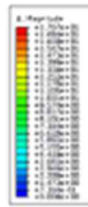
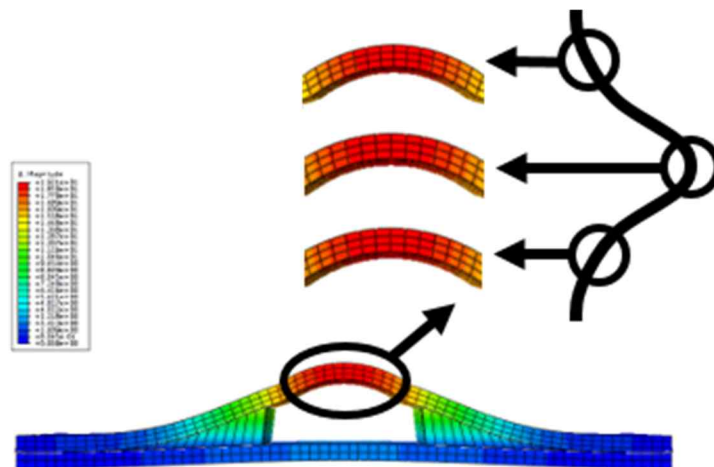


Figure 3.3 3D plate model of (a) undeformed state and deformed state for (b) perfect bonding model, (c) cohesive zone model and (d) statistical fracture model.

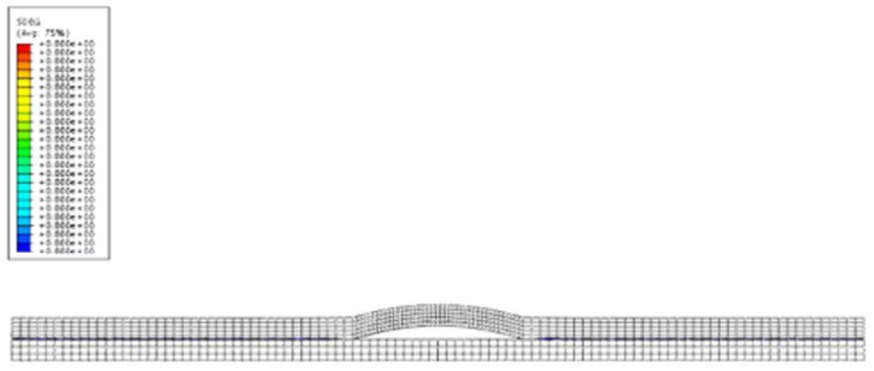


**(c) Cohesive zone model
(Simple power-law criterion)**

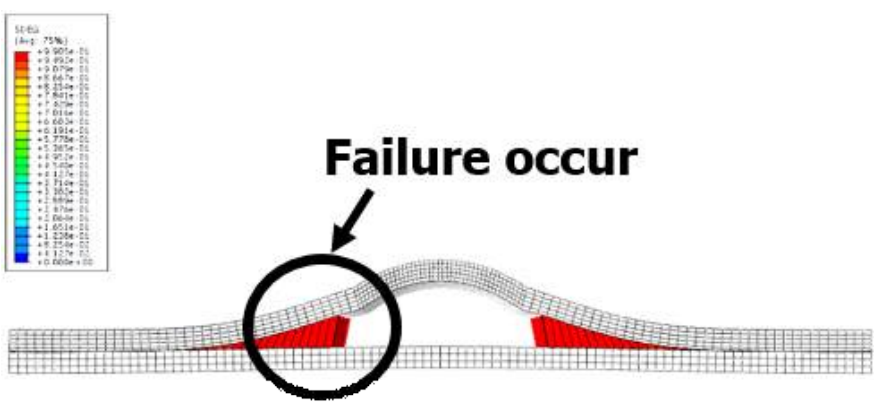


(d) Statistical fracture model

Figure 3.3 3D plate model of (a) undeformed state and deformed state for (b) perfect bonding model, (c) cohesive zone model and (d) statistical fracture model.



(a) Undeformed state



(b) Deformed state

Figure 3.4 3D plate model of (a) undeformed state and (b) deformed state of SDEG distribution.

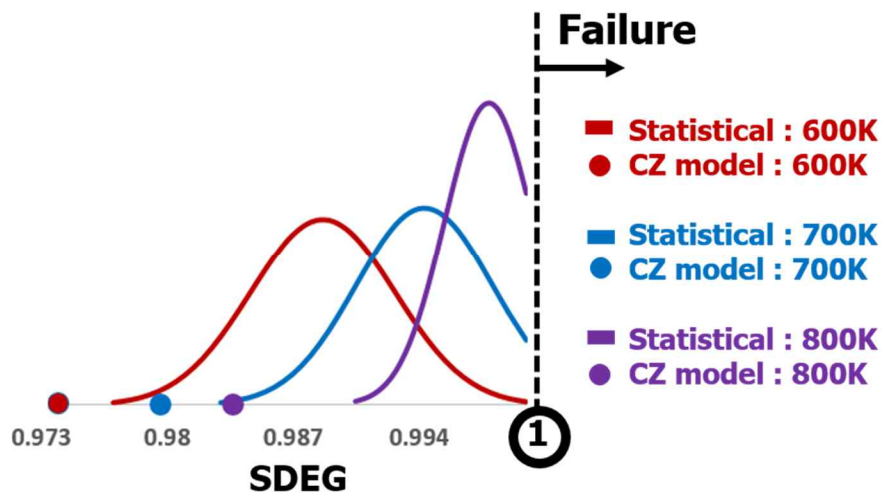
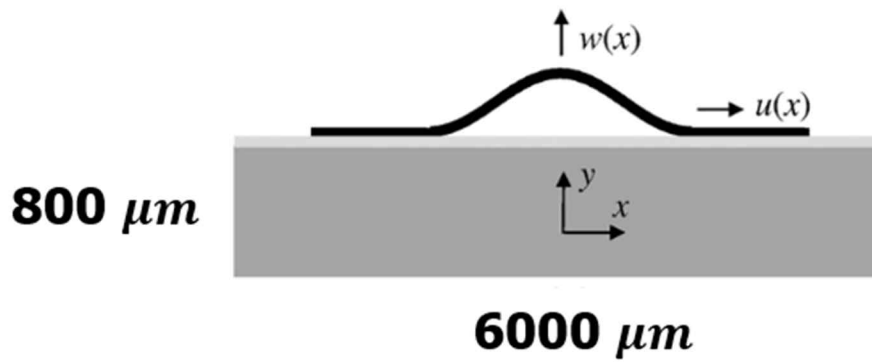
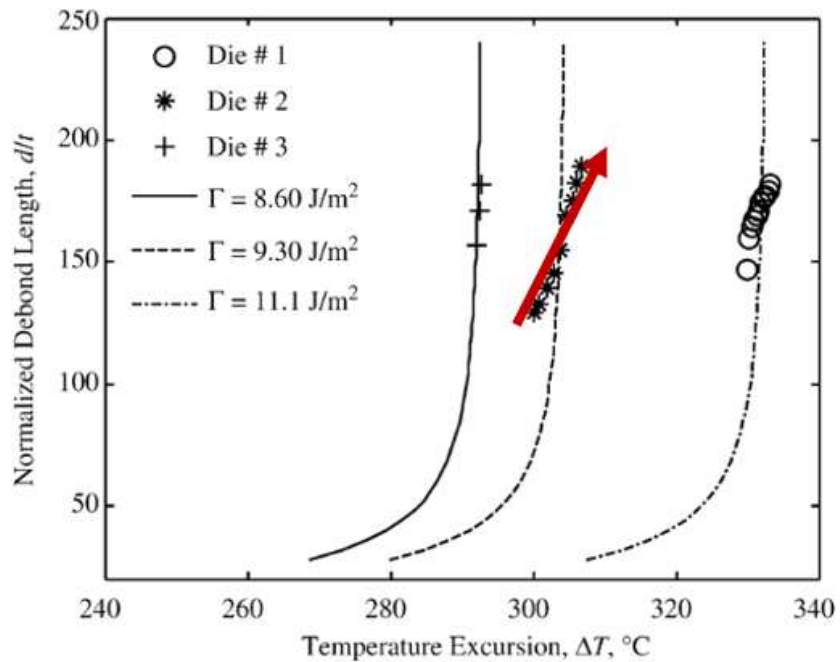


Figure 3.5 SDEG distribution comparison statistical model with cohesive zone model.



(a) Polymer-SiN substrate



(b) Debond length according to temperature

Figure 3.6 Reference data [31] of (a) Polymer-SiN substrate model and (b) Debond length according to temperature.

Table 3.1 Deformation (U) of wafer fracture model for perfect bonding model, cohesive zone model, and statistical fracture model.

| | Perfect bonding model | Cohesive zone model | Statistical fracture model |
|-------|--------------------------|------------------------|-------------------------------|
| T (K) | U (mm) | U (mm) | U (mm) |
| 600 | 0.82 | 13.26 | $N(15.26, 0.80^2)$ |
| 700 | 1.12 | 15.59 | $N(16.98, 1.02^2)$ |
| 800 | 1.37 | 17.67 | $N(20.07, 1.31^2)$ |

Table 3.2 SDEG of wafer fracture model for perfect bonding model, cohesive zone model, and statistical fracture model.

| | Perfect bonding model | Cohesive zone model | Statistical fracture model |
|-------|--------------------------|------------------------|-------------------------------|
| T (K) | SDEG | SDEG | SDEG |
| 600 | N/A | 0.9740 | $N(0.9912, 0.0052^2)$ |
| 700 | N/A | 0.9797 | $N(0.9954, 0.0036^2)$ |
| 800 | N/A | 0.9837 | $N(0.9987, 0.0025^2)$ |

Table 3.3 Yield rate of wafer fracture model for perfect bonding model, cohesive zone model, and statistical fracture model.

| | Perfect bonding model | Cohesive zone model | Statistical fracture model |
|-------|-----------------------|---------------------|----------------------------|
| T (K) | Yield rate (%) | Yield rate (%) | Yield rate (%) |
| 600 | 100 | 100 | 95.82 |
| 700 | 100 | 100 | 91.75 |
| 800 | 100 | 100 | 78.81 |

Table 3.4 Comparison of normalized debond length on wafer film among reference data and fracture models.

| Model | Ref. | | Perfect bonding model | | Cohesive zone model | | Statistical fracture model | |
|---------|------|-----|-----------------------|-----|---------------------|--------|----------------------------|--------|
| T(K) | 573 | 583 | 573 | 583 | 573 | 583 | 573 | 583 |
| L (d/t) | 130 | 190 | 0 | 0 | 130 | 158.89 | 130 | 203.18 |

Chapter 4

Conclusions

The wafer fracture model is organized to propose the fracture analysis of laminated wafer structure, considering uncertainties of material properties and interfacial fracture properties. Because thickness of laminated wafer structure is very thin, so uncertainty issues for material and interfacial properties are approached. The uncertainties of those properties has a great effect on the failure of laminated wafer structure. In this study, a statistical molecular dynamics simulations are proposed to express the uncertainties of material and interfacial properties at the nano-scale. Through those statistical atomic models, the thermo-mechanical properties of wafer materials and interfacial fracture properties are defined as a normal distribution function. In particular, to interpret the uncertainties of interfacial properties, 17250 number of T-S data points are calculated and the distribution is analyzed. In the

elastic region, dispersion of data sets is small, but the dispersion of plastic failure region is large. As a result, especially the dispersion of toughness is much larger than other fracture properties. In order to verify the statistical-based interpretation of the fracture properties, it is confirmed that it was within the error range through comparison with experimental data. Base on those statistical properties. The statistical fracture criterion at the interface of wafer film is newly defined through Monte-Carlo simulations. Normal distribution functions of those characteristics are provided considering the uncertainties of wafer characteristics by using molecular dynamics simulations.

Based on those probability distributions, a finite element model for laminated wafer structure is constructed through the cohesive zone model. The cohesive zone model is constructed by implementing the statistical bridging method to investigate the fracture behavior of system in continuum scale based fracture properties obtained from MD simulations. In order to consider those statistical material and interfacial distributions together, in this study, a Monte-Carlo simulations are performed and a statistical-based fracture analysis model is newly suggested. Statistical fracture results provide not only numerical solutions with reliability bounds in continuum scale but also error range and failure rate of the wafer system.

3D plate model is designed to simulation model of wafer film, which is most used wafer simulation model. Based on the finite element model, the proposed wafer fracture model is compared with existing fracture model of perfect bonding

model and cohesive zone model based simple power-law criterion. The degree of deformation and fracture behavior under thermal stress for each wafer fracture model are compared. In the case of the perfect bonding model, interfacial failure does not occur due to the bonding condition, and thus shows a different deformation trend than other models. In the case of the cohesive zone model based simple power-law criterion, it shows a similar pattern to the statistical fracture model, but the numerical value is slightly different and it is derived as a single analysis value. In the case of the proposed statistical fracture model, fracture analysis values are provided in the form of a normal distribution, so that the analysis average value and its error range can be presented together. Furthermore, through comparison with reference data based on experimental fracture analysis, it is confirmed that the model proposed in this study presented a more accurate fracture phenomenon than the existing wafer fracture model of perfect bonding model and cohesive zone model based simple power-law criterion.

Appendix A

Traction-Separation Curves by MD Simulations

A.1 Overview

In order to investigate the fracture analysis on the interface of laminated composite structure, the traction-separation model is considered to characterize the interfacial fracture properties by molecular dynamics simulations. In this study, the traction-separation model of SiN/SiO₂ was constructed in the form of bi-layer model by combining above validated unit cells in this study. The bi-layer model was performed by three types of fracture tensile simulations for normal mode, shear mode, and mixed mode to identify traction-separation curves for each fracture mode.

A.2 Traction-Separation for Temperature and Tensile Rate

By the way, there are essential simulation parameters when performing the tensile simulation, which are a temperature and a tensile rate speed. Those parameters are also important factors in experimental fracture tests, so the correlations between fracture toughness and corresponding factors are identified for various laminated composite materials. The variation of fracture toughness depending on temperature for different laminated composite materials as shown in Fig. A.2.1 (a) and (b), and Fig. A.2.1 (c) described the variation of toughness according to tensile rate speed [31, 32]. Although each composite material has a different detailed tendency, it could be seen that the difference in toughness is not large in common depending on temperature, also it could be confirmed that the toughness tends to converge as the tensile rate decreases.

Consequently, normal tensile simulations for corresponding parameters are performed using the proposed bi-layer model in this study before performing tensile simulations for each fracture mode. Those tensile simulations were carried out for the bi-layer system by using the Large-Scale Atomic/Molecular Massively Parallel Simulator (LAMPPS, Sandia Lab). First, tensile simulations are performed on the proposed model under the temperature conditions of 0K, 100K, 300K, and 1000K. Traction-separation curves for each temperature are depicted in Fig. A.2.2 (a). It is seen that the change in fracture toughness is within the margin of error in 0K to 300K but the property highly decreases with the temperature of 1000K. Accordingly, the

temperature condition was set to 0K in future tensile simulations because the error was not large compared to the room temperature even with the curve at 0K. Additionally, the T-S curve at 0K is the most stable and has less fluctuation, resulting in less error in obtaining fracture properties. Second, fracture simulations are performed on the MD model under the tensile rate conditions of 0.15, 0.2, 0.25, and 0.5. Those rate values means the pulling distance per simulation step, besides the parameter of 0.2nm corresponds to $10^9/s$, which is generally used in MD simulations. T-S curves for each tensile rate are depicted in Fig. A.2.2 (b), and toughness for what are also tabulated in table 3 under 0K. It is confirmed that the T-S curve converged as the tensile rate decreases, hence the tensile rate condition was set to 0.2 in future fracture simulations. Moreover, the tendency of simulation results according to temperature and tensile rate is similar to that of experimental results which is presented in Fig. A.2.2. Consequently, the tensile simulations were performed for normal mode, shear mode, and mixed mode under the tensile rate of 0.2 at quasi steady state in this study.

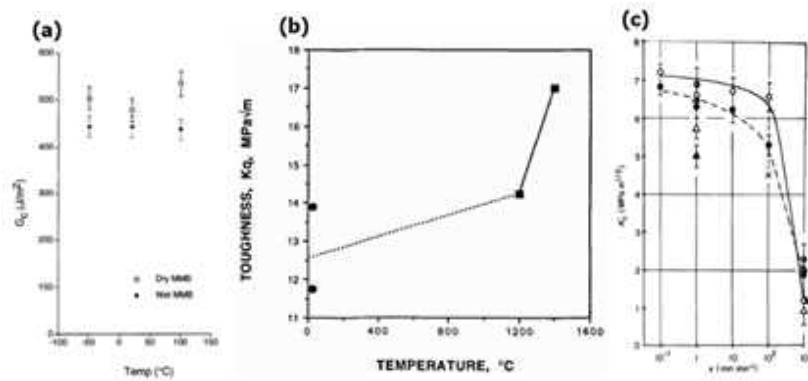
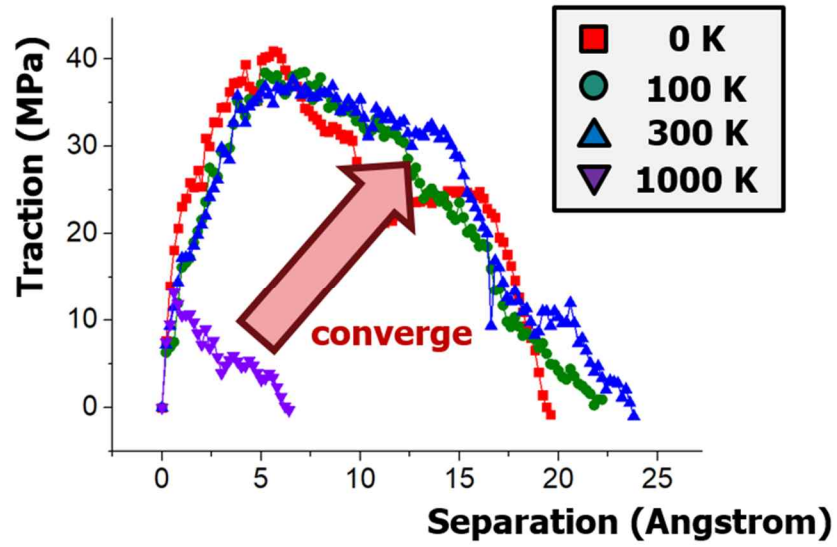
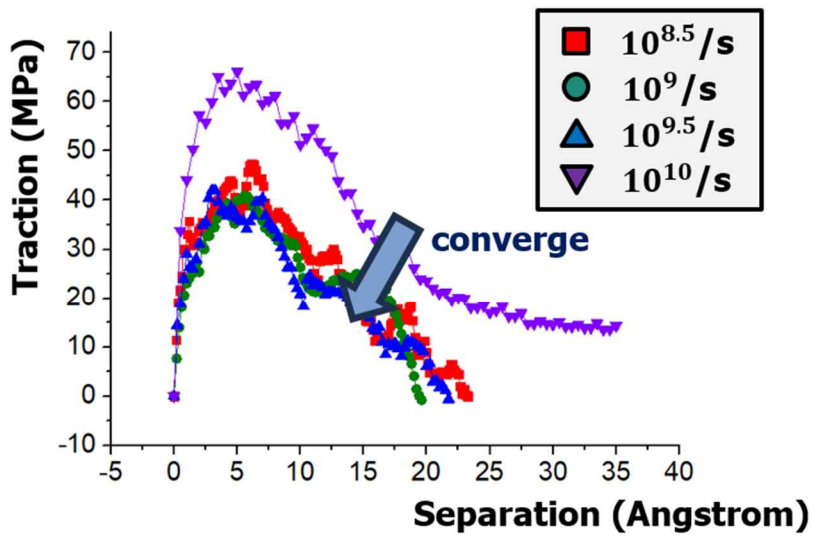


Figure A.2.1 Fracture toughness curves according to (a) and (b) temperature, and (c) tensile rate [31, 32].



(a) T-S curves for 0K, 100K, 300K, and 1000K



(b) T-S curves for $10^{8.5}/s$, $10^9/s$, $10^{9.5}/s$, $10^{10}/s$

Figure A.2.2 T-S curves for (a) temperatures and (b) tensile rates.

A.3 Characterization of Mixed-Mode Cohesive Law

The mixed-mode cohesive law is characterized by two-step fracture criterions according to fracture stages, which are damage initiation region and damage evolution region. The damage initiation region is the elastic stage where the interface of laminated composite structure is introduced in the linear elastic loading. Also damage evolution region is defined after critical point under the conditions of failure softening stage.

In the damage initiation region, it is satisfied that the fracture damage is progressed when the quadratic stress criterion is considered as [33]:

$$\left(\frac{\tau_{Nim}}{\tau_{Ni}}\right)^2 + \left(\frac{\tau_{Sim}}{\tau_{Si}}\right)^2 \leq 1 \quad (7)$$

Where τ_{Nim} and τ_{Sim} are traction stresses according to the mixed-mode separation for normal and shear directions. Because of the linear elastic relation between traction stress and separation in this fracture region, Eq. (7) was rewritten in separation terms as:

$$\left(\frac{\delta_{Nim}}{\delta_{Ni}}\right)^2 + \left(\frac{\delta_{Sim}}{\delta_{Si}}\right)^2 \leq 1 \quad (8)$$

Where δ_{Nim} and δ_{Sim} are mixed-mode separation distances for normal and shear directions corresponding to τ_{Nim} and τ_{Sim} , respectively. The slip separation of mixed-mode state (δ_{mim}) is defined as:

$$\delta_{mim}^2 = \delta_{Nim}^2 + \delta_{Sim}^2 \quad (9)$$

Subsequently, the loading angle (β) is determined as the ratio of the normal and shear

separation distances as follows:

$$\beta = \frac{\delta_{Sm}}{\delta_{Nm}} \quad (10)$$

The decomposed slip separations for normal direction (δ_{Nm}) and shear direction (δ_{Sm}) according to loading angle (β) are obtained by using Eq. (8) and (10), which is as follows:

$$\delta_{Nm} = \frac{\delta_{Ni}\delta_{Si}}{\sqrt{\delta_{Si}^2 + \beta^2\delta_{Ni}^2}} \quad (11)$$

$$\delta_{Sm} = \frac{\beta\delta_{Ni}\delta_{Si}}{\sqrt{\delta_{Si}^2 + \beta^2\delta_{Ni}^2}} \quad (12)$$

Therefore, Eq. (11) and Eq. (12) were substituted for Eq. (9) to describe the mixed-mode initial separation (δ_{mi}) according to loading angle, which is defined as:

$$\delta_{mi} = \delta_{Ni}\delta_{Si} \sqrt{\frac{1 + \beta^2}{\delta_{Si}^2 + \beta^2\delta_{Ni}^2}} \quad (13)$$

After the damage initiation process, the failure softening is progressed in the damage evolution region. In the softening stage, diverse fracture criteria such as power law criterion [34], B-K criterion [35], and PPR potential [36] have been used to investigate the damage propagation behavior in many researches. In this study, power law criterion is considered to investigate the damage evolution since the criterion have been generally used in many material systems, which is satisfied as [37]:

$$\left(\frac{G_{Nm}}{G_N}\right)^\alpha + \left(\frac{G_{Sm}}{G_S}\right)^\alpha \leq 1 \quad (14)$$

Where G_{Nm} and G_{Sm} are fracture toughness according to the mixed-mode

separation for normal and shear directions, respectively, α is the mode mixity describing the slop of power law criterion. The mode mixity is characterized by fracture toughness points of normal mode, shear mode, and mixed mode. In this study, the mode mixity is determined by toughness points which are described for proposed fracture mode by MD simulations as shown in Fig. A.3.1

Furthermore, fracture toughness of mixed mode state for normal direction (G_{Nm}) and shear direction (G_{Sm}) are calculated as:

$$G_{Nm} = \int_0^{\delta_{Nfm}} \tau_{Nm} d\delta_{Nm} = \frac{1}{2} k_N \delta_{Nin} \delta_{Nfm} \quad (15)$$

$$G_{Sm} = \int_0^{\delta_{Sfm}} \tau_{Sm} d\delta_{Sm} = \frac{1}{2} k_S \delta_{Sim} \delta_{Sfm} \quad (16)$$

Where δ_{Nfm} and δ_{Sfm} are decomposed final separations for normal and shear directions. Eq. (15), and Eq. (16) were substituted for Eq. (14) to investigate the final separations of each fracture mode in corresponding fracture criterion, which is described as follows:

$$\left(\frac{\frac{1}{2} k_N \delta_{Nin} \delta_{Nfm}}{G_N} \right)^\alpha + \left(\frac{\frac{1}{2} k_S \delta_{Sim} \delta_{Sfm}}{G_S} \right)^\alpha = 1 \quad (17)$$

$$\left(\frac{1}{2} \delta_{Nin} \delta_{Nfm} \right) \left[\left(\frac{k_N}{G_N} \right)^\alpha + \left(\frac{\beta^2 k_S}{G_S} \right)^\alpha \right] = 1$$

Decomposed final separations for normal direction (δ_{Nfm}) and shear direction (δ_{Sfm}) are determined by Eq. (17):

$$\delta_{Nfm} = \frac{2}{\delta_{Nim}} \left[\left(\frac{k_N}{G_N} \right)^\alpha + \left(\frac{\beta^2 k_S}{G_S} \right)^\alpha \right]^{-\frac{1}{\alpha}} \quad (18)$$

$$\delta_{Sfm} = \frac{2\beta}{\delta_{Nim}} \left[\left(\frac{k_N}{G_N} \right)^\alpha + \left(\frac{\beta^2 k_S}{G_S} \right)^\alpha \right]^{-\frac{1}{\alpha}} \quad (19)$$

Thus, final separation of mixed mode state (δ_{mf}) according to loading angle is determined by Eq. (18), and (19), which is described as:

$$\delta_{mf} = \frac{2(1 + \beta^2)}{\delta_{mi}} \left[\left(\frac{k_N}{G_N} \right)^\alpha + \left(\frac{\beta^2 k_S}{G_S} \right)^\alpha \right]^{-\frac{1}{\alpha}} \quad (20)$$

Fracture properties of mixed-mode state such as fracture toughness (G_m), critical traction stress (τ_m), and fracture stiffness (k_m) are determined according to loading angle since the mixed-mode cohesive law is organized by characterizing the quadratic stress criterion in initiation region and the power law criterion in evolution region. The fracture toughness for normal direction (G_{Nm}) and shear direction (G_{Sm}) are investigated by substituting Eq. (11), (12), (18), and (19) into Eq. (15) and (16), which is described as:

$$G_{Nm} = k_N \left[\left(\frac{k_N}{G_N} \right)^\alpha + \left(\frac{\beta^2 k_S}{G_S} \right)^\alpha \right]^{-\frac{1}{\alpha}} \quad (21)$$

$$G_{Sm} = \beta^2 k_S \left[\left(\frac{k_N}{G_N} \right)^\alpha + \left(\frac{\beta^2 k_S}{G_S} \right)^\alpha \right]^{-\frac{1}{\alpha}} \quad (22)$$

Therefore the fracture toughness of mixed-mode state (G_m) is investigated by the sum of G_{Nm} and G_{Sm} , which is as follows:

$$G_m = (k_N + \beta^2 k_S) \left[\left(\frac{k_N}{G_N} \right)^\alpha + \left(\frac{\beta^2 k_S}{G_S} \right)^\alpha \right]^{-\frac{1}{\alpha}} \quad (23)$$

Moreover, traction-separation curves for mixed mode failure are obtained in a bi-linear curve since the proposed mixed-mode cohesive law was organized by using bi-linear fitting curve of traction-separation curve for normal mode, shear mode, and mixed mode. Hence, the critical traction stress for mixed mode (τ_m) is calculated as follows:

$$\tau_m = \frac{2G_m}{\delta_{m f}} \quad (24)$$

The fracture stiffness of mixed mode state (k_m) is also determined by dividing the critical stress by the suggested mixed-mode initial separation ($\delta_{m i}$), which is described as:

$$k_m = \frac{\tau_m}{\delta_{m i}} \quad (25)$$

Mixed mode cohesive law analysis was performed based on quadratic stress criterion and power law criterion, so mixed mode fracture properties (G_m , τ_m , k_m) were determined according to loading angle through Eq. (23), (24), and (25).

Based on those physical quantities presented in Table A.3.1 and A.3.2, the fracture toughness for each fracture mode are calculated and presented as green points according to loading angle in Fig. A.3.2. The power law criterion is fitted to determine the mode mixity of the wafer system based on those properties, and this fitting process is also illustrated in Fig. A.3.2. The violet graph is finally determined power law criterion and its mode mixity is 0.552 as shown in Fig. A.3.2. The mixed mode cohesive law on the interface of wafer film is established by corresponding characteristics and the mode mixity, which is depicted in Fig. A.3.3 (a). It is proposed that the T-S curve criterion is determined according to loading angle, so those

responses could be derived by the criterion for any loading angle (0 degree to 90 degree). Therefore, T-S responses for loading angles of 20 degree, 60 degree, and 80 degree are calculated by the cohesive law as an example providing fracture quantities for each angle, which is illustrated in Fig. A.3.3 (b).

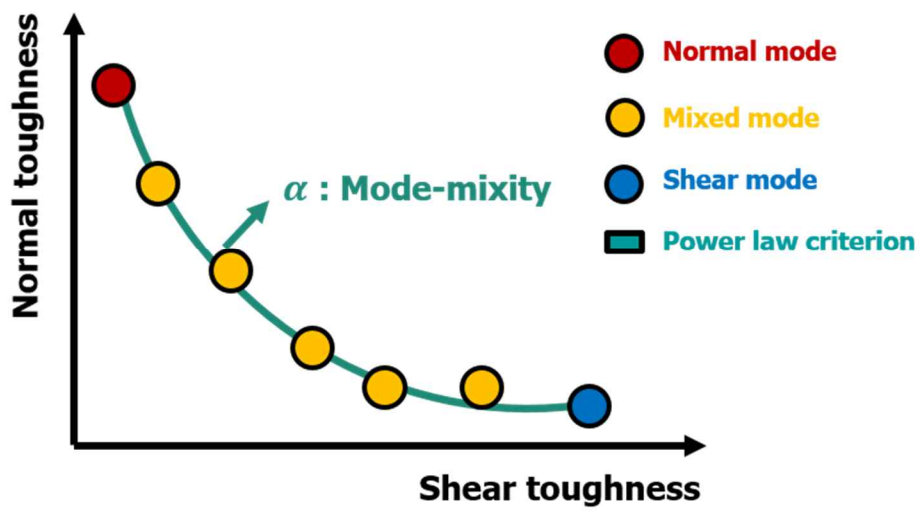


Figure A.3.1 Schematic diagram of determining mode-mixity

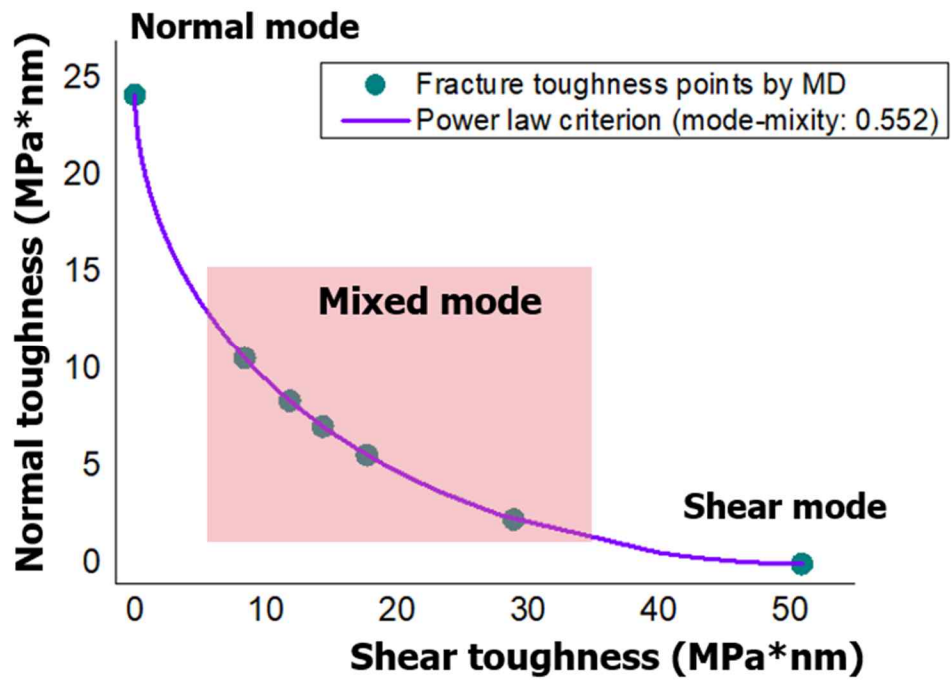
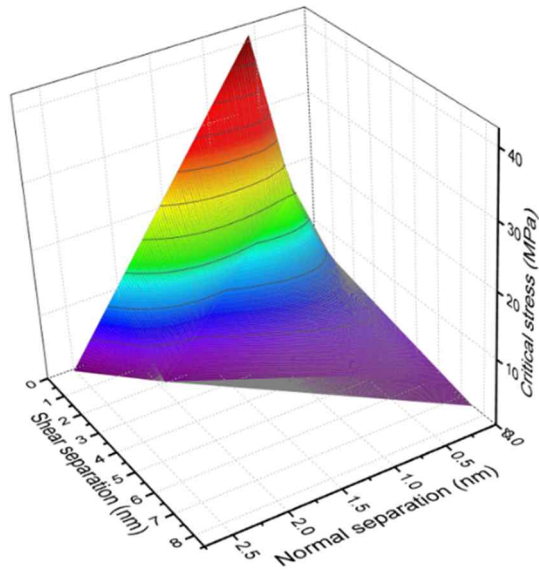
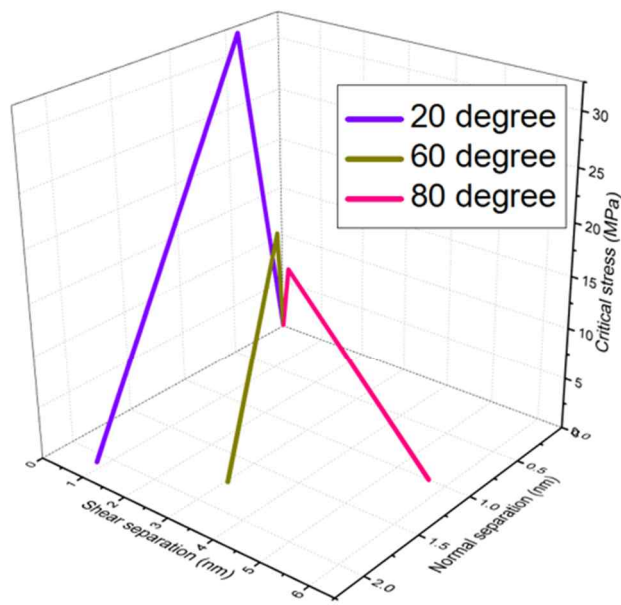


Figure A.3.2 Determine mode mixity by power law criterion.



(a) Mixed-mode cohesive law



(b) T-S curves obtained by cohesive law

Figure A.3.3 (a) Mixed mode cohesive law and its (b) T-S curves.

Table A.3.1 Fracture properties for normal direction derived by MD.

| Fracture mode | Angle (Degree) | Fracture properties for normal direction | | |
|---------------|----------------|--|-----------------------|--------------------|
| | | Fracture stiffness (MPa/nm) | Critical stress (MPa) | Toughness (MPa*nm) |
| Normal mode | 0 | 73.1 | 40.93 | 50.87 |
| Mixed mode | 26.57 | 67.9 | 31.22 | 23.54 |
| Mixed mode | 45 | 60.1 | 36.08 | 23.15 |
| Mixed mode | 51.34 | 66.7 | 28.32 | 19.39 |
| Mixed mode | 56.31 | 71.4 | 25.71 | 12.61 |
| Mixed mode | 63.43 | 62.5 | 15.00 | 11.91 |
| Shear mode | 90 | 0 | 0 | 0 |

Table A.3.2 Fracture properties for shear direction derived by MD.

| Fracture mode | Angle (Degree) | Fracture properties for shear direction | | |
|---------------|----------------|---|-----------------------|--------------------|
| | | Fracture stiffness (MPa/nm) | Critical stress (MPa) | Toughness (MPa*nm) |
| Normal mode | 0 | 0 | 0 | 0 |
| Mixed mode | 26.57 | 23.2 | 5.56 | 4.17 |
| Mixed mode | 45 | 7.9 | 3.34 | 1.36 |
| Mixed mode | 51.34 | 13.3 | 4.78 | 3.21 |
| Mixed mode | 56.31 | 13.4 | 5.35 | 7.57 |
| Mixed mode | 63.43 | 33.1 | 6.63 | 4.84 |
| Shear mode | 90 | 23.0 | 6.45 | 24.15 |

Appendix B

Effective Thickness of Cohesive Zone

Element

B.1 Overview

Cohesive zone model have been mainly used to characterize the fracture mechanism on laminated composite structures. In particular, it is dominant issue in the analysis model that determining the cohesive zone element which investigate the fracture behavior. Cohesive parameters are calculated by MD simulations in this study, which are defined as fracture properties. However, these corresponding properties depend on the slab length of the bi-layer model. Therefore, defining the effective length of cohesive zone element according to slab length is important for

constructing the cohesive zone model that reflects those characteristics of fracture properties. Therefore, the correlation between T-S curve and slab length is investigated, also it is identified that the influence of slab length on length of cohesive element. Furthermore, it is discussed how to determine the effective length of cohesive zone element. Besides, the cohesive zone model of wafer is proposed through those corresponding parameters by using the multiscale simulation framework.

B.2 Interface Slab Length Effect for Bi-Layer Model

The bi-layer model is constructed to obtain T-S curves on the interface of wafer film by MD simulations, which is described. The T-S responses are derived from the interface slab illustrated as the blue zone in the bi-layer model, which is depicted in Fig. 24. By the way, those responses are differently calculated according to the interface slab length, which is identified that interfacial failure properties depend on how the interface slab is defined. It is seen that T-S curves depend on the length of interface slab in the case of the graphene/polymer composite structure. In general, the high toughness is obtained from T-S curves when the interface slab length of the bi-layer model is short. Thus, normal tensile simulations are implemented on bi-layer models for 3.5nm, 4.5nm, 5.5nm, 6.5nm, and 7.5nm of interface slabs in order to confirm the slab length effect in this study. T-S curves for each slab length are described in Fig. B.2.1 and those fracture properties for each

curve are tabulated in table B.2.1. Fig. B.2.1 indicates that T-S responses show exponential softening behavior when the slab length is short because interfacial non-bond interactions such as van der waals interactions and electrostatic interactions are dominant factors in the short slab region which is inversely proportional to the separation. Accordingly, the critical stress and fracture toughness for short slab length are extremely high as shown in the graphs for 2.5nm and 3.5nm in Fig. B.2.1. On the other side, T-S curves represent linear softening failure under the conditions of long slab length as shown in Fig. B.2.1, which indicates that interfacial non-bond interaction effects combine with the plastic failure effects of materials in the long slab region. Fracture toughness for short slab region is low since the material failure effect is higher when the length is short, which is described as the graphs for 5.5nm, 6.5nm, and 7.5nm in Fig. 5.1. Hence, the T-S curve on the interface of wafer is determined by interfacial non-bond interaction effect and material failure effect according to interface slab length.

However, final continuum analysis derived from cohesive zone model should be identical for different conditions of slab length since it is a fracture phenomenon that occurs in the same material composite system. This results refers to the need for defining an effective length of cohesive zone element that reflect the proposed slab length effect. The previous cohesive zone elements were set to reasonably thin length such as a hundredth of the model thickness or assumed to be zero thickness when constructing the cohesive zone model for laminated composite structures. However, an effective length of cohesive zone element is determined

according to interface slab length in this study to construct the cohesive zone model for wafer film that could identify the interfacial fracture characteristics regardless of the circumstance of the slab length effect. Therefore, a cohesive zone model is designed to the DCB test specimen model to simulate an interfacial normal test by many studies [38], which is illustrated in Fig. B.2.2. The thickness of the cohesive zone element is designed at 0.55mm in this model to reflect the interface slab length of 5.5nm, which is approximately 1/60 of the overall system thickness. The cohesive parameters are also determined by those fracture properties from the slab length of 5.5nm in the model. The model is a numerical analysis model mainly used to investigate the normal fracture mechanism on the interface of a laminated composite structure by pulling materials equally at each step, which is depicted in Fig. B.2.3 (a) and (b). Fig. 5.2.3 (a) shows the stress distribution of the model with pulling distance, also Fig. 5.2.3 (b) represents the SDEG distribution on the cohesive zone according to distance. SDEG is an ABAQUS built in function that indicates whether or not the cohesive zone element is destroyed, and the zone is failure if the SDEG value is 1. It is seen that SOH polymer is applied under a lower stress distribution than SiN because the polymer is relatively soft material, and the interfacial failure is indicated at pulling distance of 11.5mm.

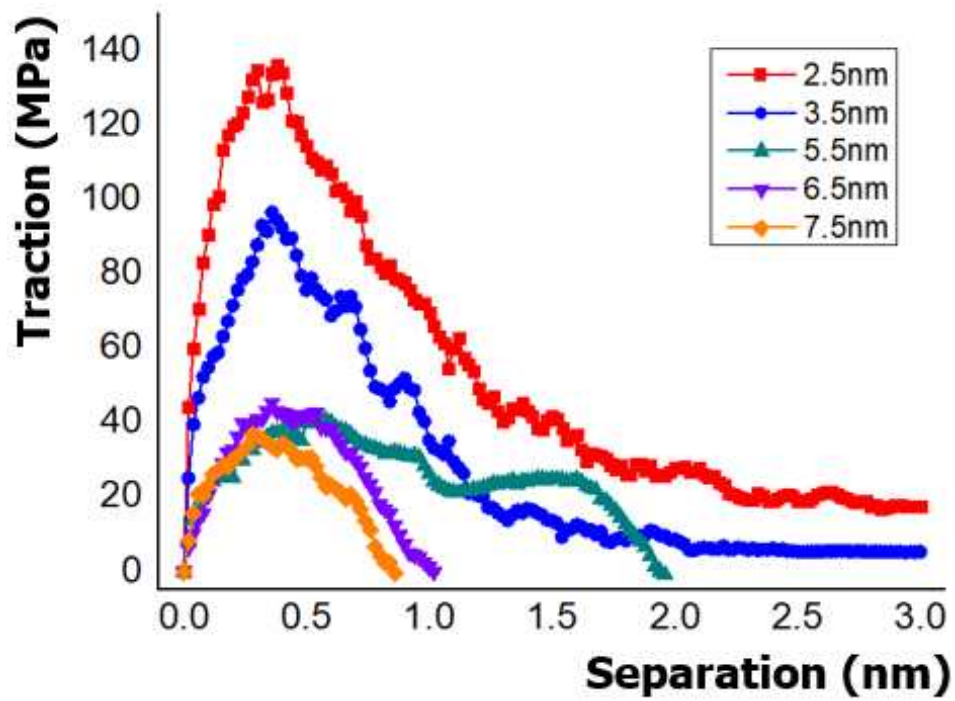


Figure B.2.1 T-S curves for slab lengths of 2.5nm, 3.5nm, 5.5nm, 6.5nm, 7.5nm.

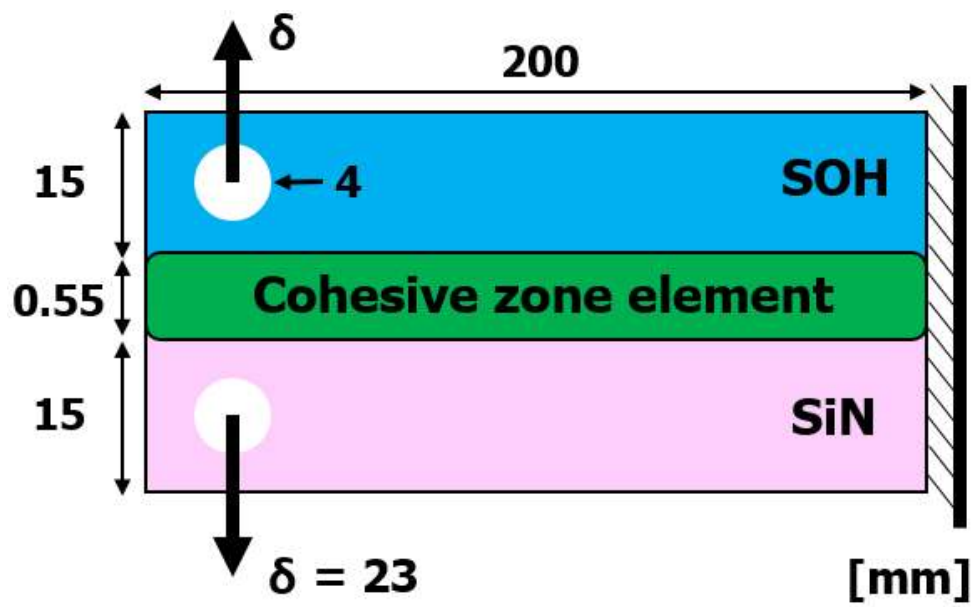
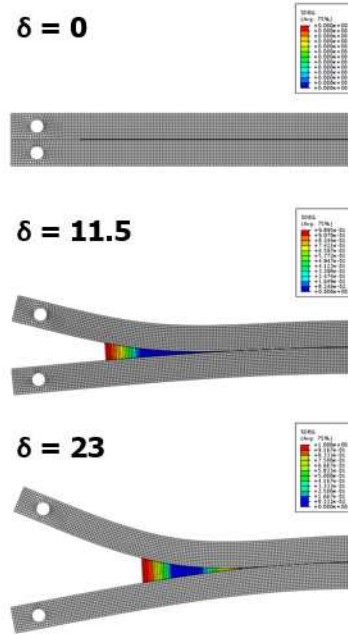
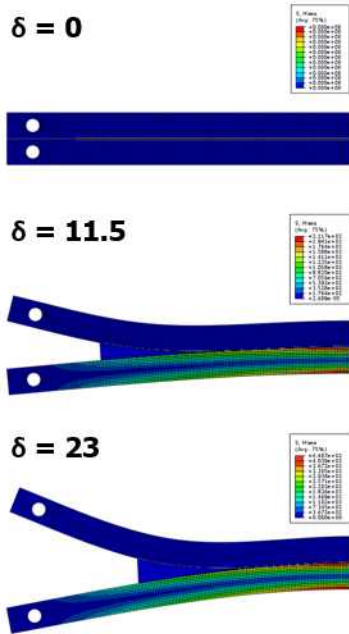


Figure B.2.2 Schematic diagram for simple normal test.



(a) Stress distribution

(b) SDEG distribution

Figure B.2.3 Cohesive zone model for (a) stress distribution and (b) SDEG distribution.

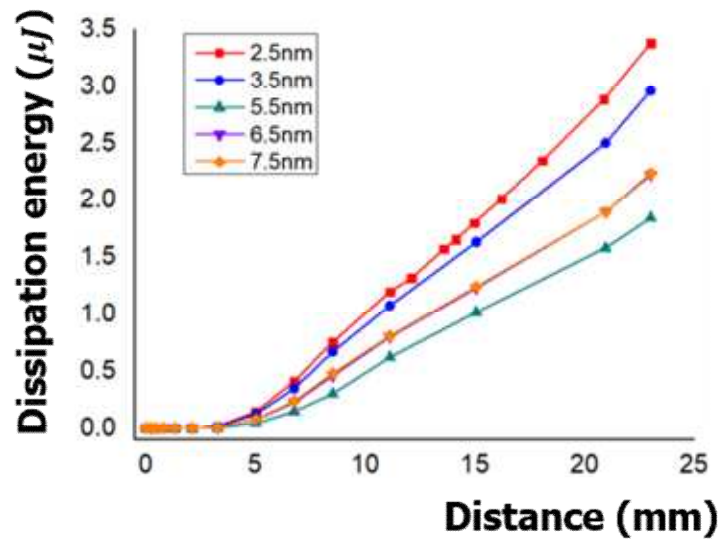
Table B.2.1 Fracture properties for different slab lengths of 2.5nm, 3.5nm, 5.5nm, 6.5nm, and 7.5nm.

| Slab length (nm) | 2.5 | 3.5 | 5.5 | 6.5 | 7.5 |
|-----------------------------|---------|---------|--------|--------|--------|
| Fracture toughness (MPa*nm) | 2339.72 | 1183.57 | 508.71 | 277.52 | 203.17 |
| Critical stress (MPa) | 136.03 | 96.47 | 40.93 | 45.29 | 36.73 |
| Fracture stiffness (MPa/nm) | 35.79 | 26.79 | 7.31 | 12.58 | 13.12 |

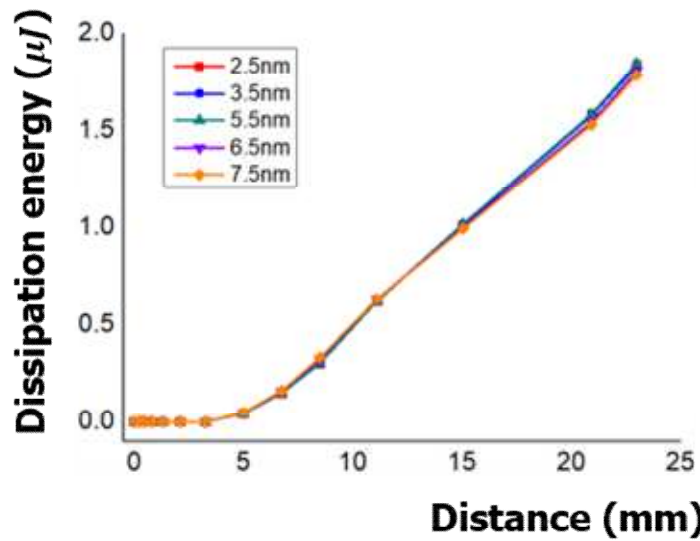
B.3 Determine effective thickness of cohesive zone elements

In order to investigate the interfacial failure according to the interface slab length, fracture properties of Table 6 with slab length are used to determine the cohesive zone model with cohesive zone thickness fixed as 0.55mm. The dissipation energy at the cohesive zone is calculated according to the slab length with the pulling distance, which is as described in Fig. B.3.1 (a). The energy increases with the distance after approximately 3.5mm, which means that the plastic deformation is developed on the interface after 3.5mm. The cohesive parameters differ depending on the slab length, which results in the difference of the dissipation energy on the interface as shown in Fig. B.3.1 (a). In particular, the influence of fracture stiffness on the energy is significant, which is shown in Fig. B.3.1 (a) that the dissipation energy increases with high fracture stiffness. The crack propagation on the interface is highly related to the fracture stiffness since the stiffness is described as a spring on the cohesive zone, which results in easily damage propagation for low stiffness. Thus, thickness of the cohesive zone element is defined by adjusting the fractures stiffness ratio according to slab length based on that of 5.5nm. The above normal fracture simulations are identically performed on the cohesive zone model under the same structural condition except for cohesive zone thickness, which is newly determined as effective length of cohesive zone according to the slab length. Fig. B.3.1 (b) indicates the dissipation energy with each effective length of cohesive zone for slab length according to pulling distance. Furthermore, the dissipation energy for

same cohesive zone thickness of 0.55mm and newly refined effective length of cohesive zone is compared and tabulated in Table B.3.1. The tendency of dissipation energies with distance is identical for each slab length as illustrated in Fig. B.3.1 (b), which is investigated that the interfacial failure behavior of wafer film is identically observed on the cohesive zone model for different slab length by using effective length of cohesive zone. The refined thickness of cohesive zone for each slab length is tabulated in Table B.3.1, which shows that defining effective length of cohesive zone is required according to slab length enabling proper fracture analysis of laminated composite structure.



(a) Identical CZ length of 0.5mm



(b) Effective CZ length for slab length

Figure B.3.1 Dissipation energy for (a) fixed CZ length and (b) effective CZ length.

Table B.3.1 Dissipation energy according to CZ length for slab length.

| Slab length (mm) | Same CZ length | | Refine CZ length | |
|---------------------|-------------------|-------------------------------------|-------------------|-------------------------------------|
| | CZ length (mm) | Dissipation energy (μ J) | CZ length (mm) | Dissipation energy (μ J) |
| 2.5 | 0.55 | 3.38 | 2.45 | 1.84 |
| 3.5 | 0.55 | 2.96 | 1.83 | 1.83 |
| 5.5 | 0.55 | 1.84 | 0.55 | 1.84 |
| 6.5 | 0.55 | 2.22 | 0.86 | 1.80 |
| 7.5 | 0.55 | 2.24 | 0.89 | 1.78 |

Appendix C

Stochastic Neural Network

Constitutive model

C.1 Overview

Numerical analysis of the hyperelastic behavior of polymer materials has drawn significant interest from within the field of mechanical engineering. Currently, hyperelastic models based on the energy density function, such as the Neo-Hookean, Mooney-Rivlin, and Ogden models, are used to investigate the hyperelastic responses of materials. Conventionally, constants relating to materials were determined from experimental data by using global least-squares fitting. However, formulating a constitutive equation to capture the complex behavior of hyperelastic

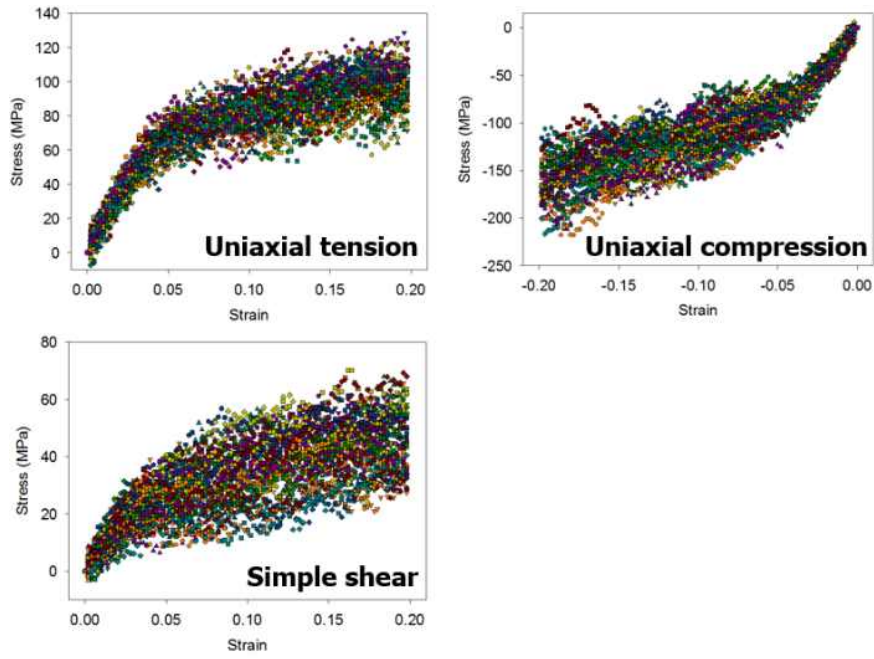
materials was difficult owing to the limitations of the analytical model and experimental data. This study addresses these limitations by using a system of neural networks (NNs) to design a data-driven surrogate model without a specific function formula, and employs molecular dynamics (MD) simulations to calculate the massive amount of combined loading data of hyperelastic materials. Thus, MD simulations were used to propose an NN constitutive model for hyperelasticity to derive the constitutive equation to model the complex hyperelastic response. Additionally, the probability distributions of the numerical solutions of hyperelasticity are used to characterize the uncertainty of the MD models. These statistical finite element results not only present numerical results with reliability ranges but also scattered distributions of the solution obtained from the MD-based probability distributions.

C.2 Statistical Stress-Strain Responses of Polymer Material

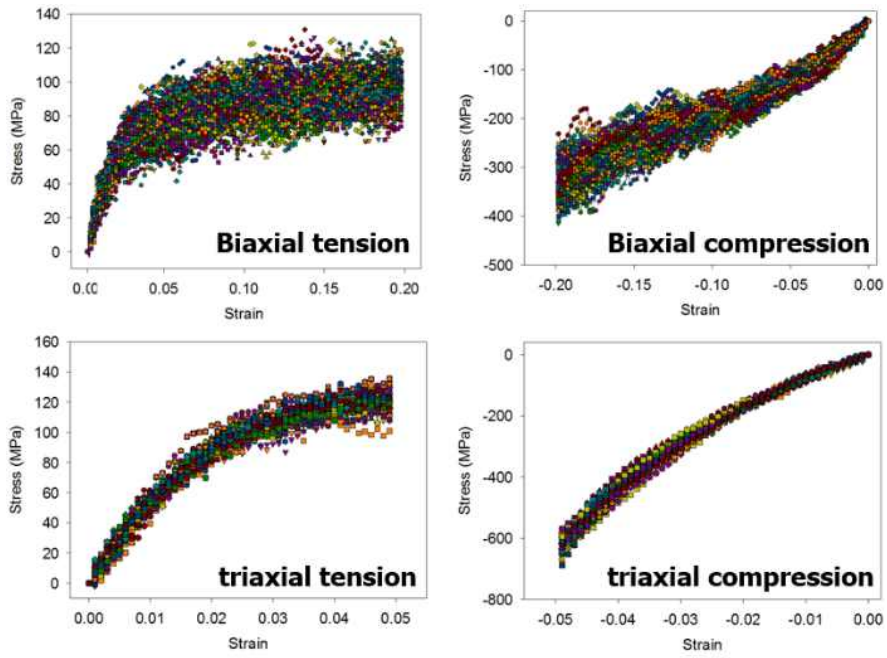
The stress–strain curves of the PS polymer that were obtained under monotonic and combined loading conditions by MD simulations are plotted in Fig. C.2.1 (a) and (b). Fig. C.2.1 (a) presents the monotonic loading data, i.e., the uniaxial tension, uniaxial compression, and simple shear, and Fig. C.2.1 (b) shows the combined loading data including the biaxial tension and compression as well as the triaxial tension and compression. The consistency of the MD cell was validated by comparing the mechanical properties derived from the MD simulations with those

that were obtained experimentally. The value of Young's modulus, which was calculated by using data from our MD simulation, is 3.38 MPa, which agrees well with the experimental data (3.0–3.5 MPa) and in the literature [39]. The equilibrated density and Poisson's ratio of the PS system obtained from our simulation data (0.95 g/cm³ 0.3707) were entirely consistent with the experimental results from other values found in the literature (0.90–0.92 g/cm³ and 0.37–0.38 [41, 42]).

The data for each type of mechanical behavior are shown in the form of a band range, as represented in Fig. C.2.1, which is necessary because of the inherent uncertainty of MD simulations. To identify the probability distribution of the stress values according to strain, the dispersion of stress was investigated, as shown in Fig. C.2.2. Those results confirmed that the stress value followed a normal distribution for each strain value, as shown by the red and green graphs in Fig. C.2.2. Based on the normal distribution data, the standard deviation of the stress for each strain value was calculated according to each loading condition. The datasets containing the data in each band range obtained from the MD simulations were converted into stochastic datasets, as shown in Fig. C.2.3 (a) and (b), using the standard deviations that were computed. The average stress and the stress with a deviation of 1 from the stress-strain curves are presented in Fig. C.2.3 (b). The 1 deviation is the variance derived from the normal distribution, suggesting that the stress values between the red and green graphs, as depicted in Fig. C.2.3 (b), represent 68.2% of the reliability range based on the mean value.



(a) Monotonic loading data



(b) Combined loading data

Fig. C.2.1 MD data of (a) monotonic and (b) combined loading.

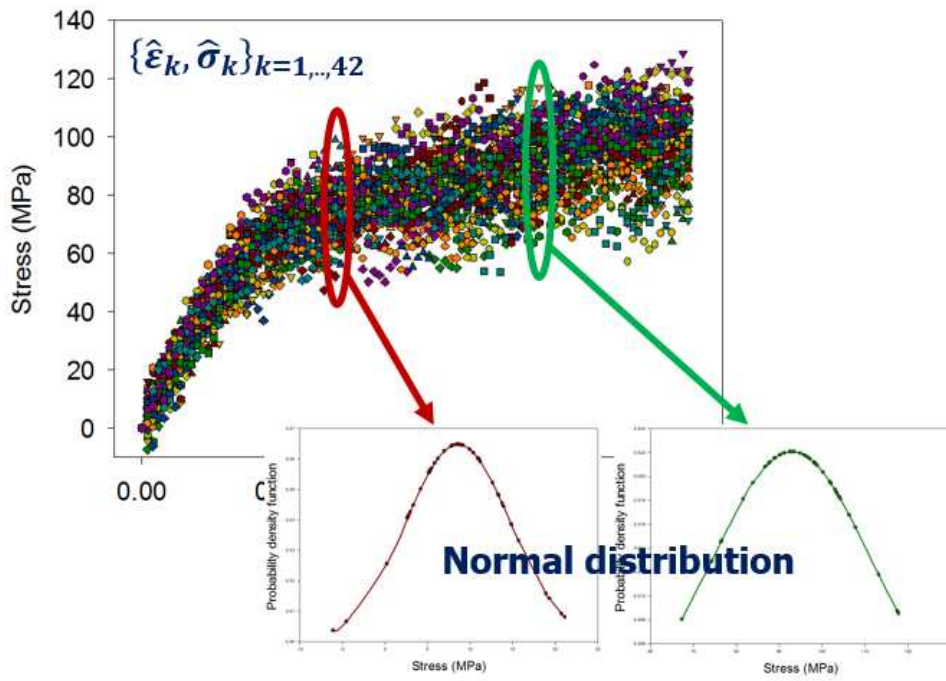
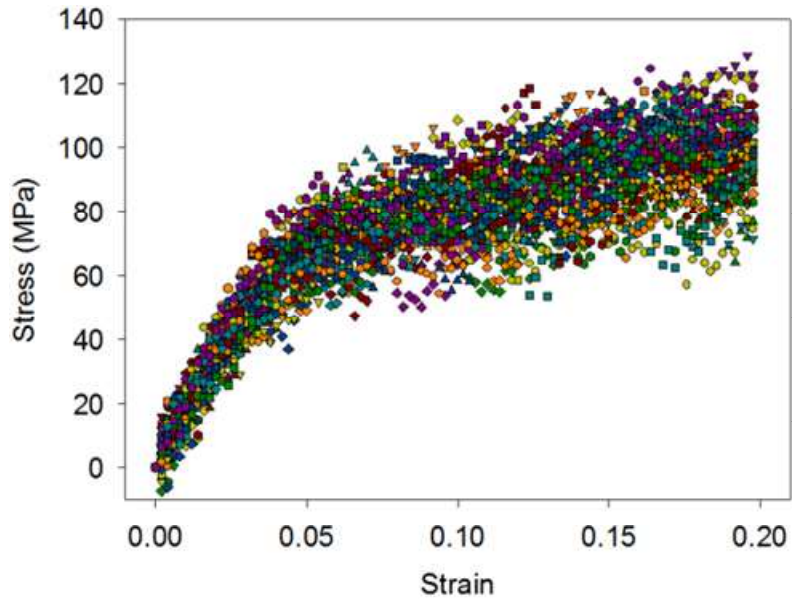
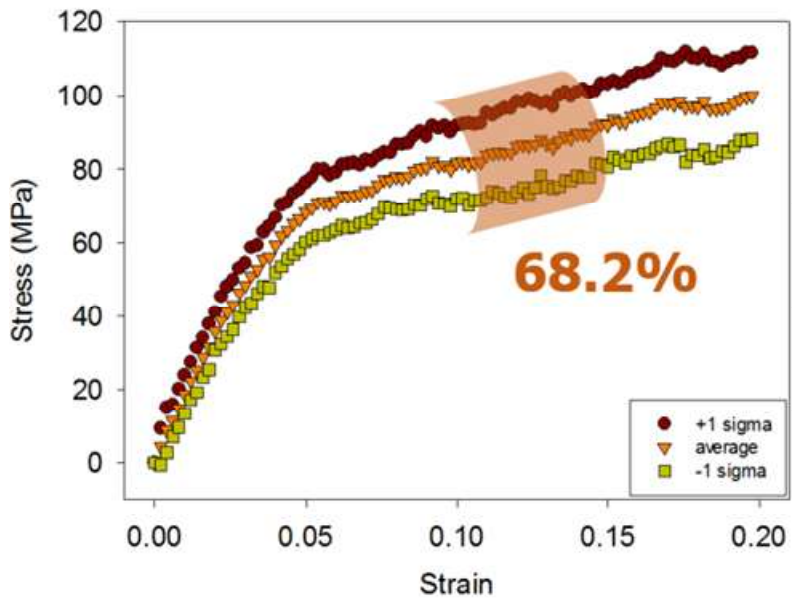


Fig. C.2.2 Normal distributions of the stress value with strain.



(a) Band gap data sets



(b) Stochastic data sets

Fig. C.2.3 Stochastic data conversion process from (a) band gap data to (b) stochastic data.

C.3 Verification of machine-learning function with hyperelasticity

The loading conditions were combined in a 1:1 ratio and the 1-D motion was inserted as input data. Then, the consistency of the model based on the machine-learning function was verified by using the training data. The results indicate that the given MD loading conditions are properly described by the function, but questions remain as to whether other types of complex behavior could also be accurately described. Additional MD simulations were implemented to verify that the model could satisfactorily predict the combined loading conditions of the polymer material in 1:2 and $-1:-2$ ratios of biaxial loading and 0.5:1:1 and $-0.5:-1:-1$ ratios of triaxial loading, as shown in Fig. C.3.1. Therefore, MD simulation data with a particular ratio were compared with the learning data derived from the hyperelastic machine-learning function, as shown in Fig. C.3.2 (a), (b), (c), and (d). The red squares and orange triangles were derived from MD simulations, and the red and black lines were produced by the machine-learning function. The stress-strain curves derived from the MD data and learning data were compared under these circumstances with 1:2 and $-1:-2$ ratios, as shown in Fig. C.3.2 (a) and (b), and they were also compared in 0.5:1:1 and $-0.5:-1:-1$ ratios, as depicted in Fig. C.3.2 (c) and (d). A comparison of the stress-strain responses indicates a reasonably good fit, which implies that the hyperelastic machine-learning function appropriately predicts the complex mechanical behavior of the material.

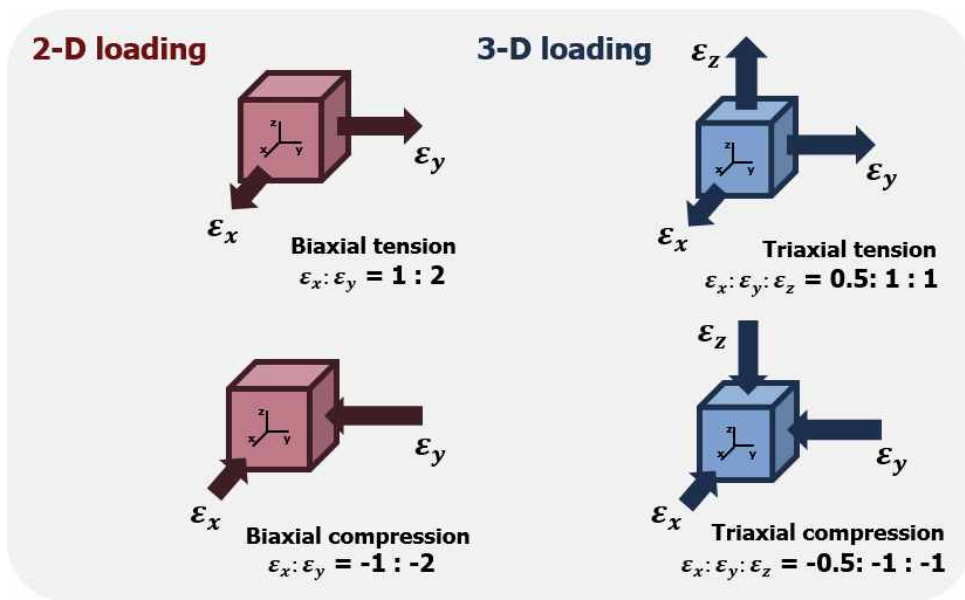
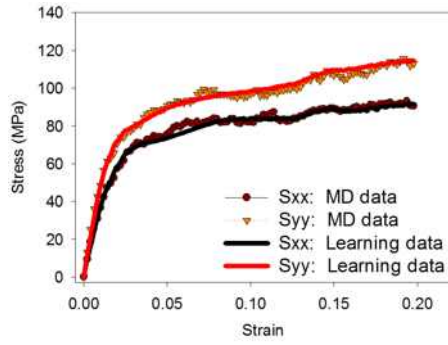
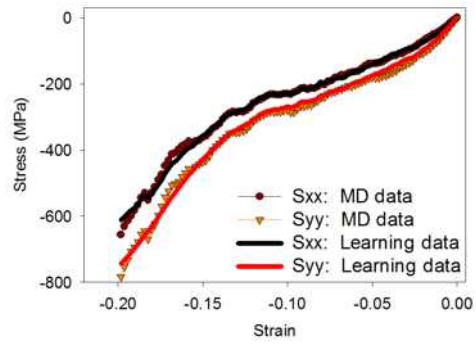


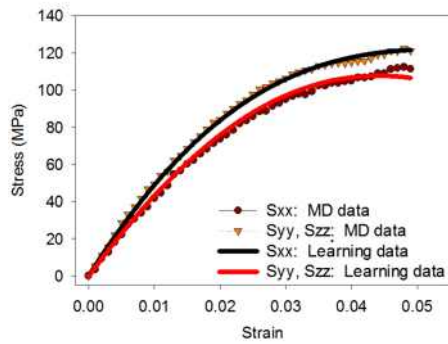
Fig. C.3.1 Additional combined loading conditions of 2-D and 3-D behaviors.



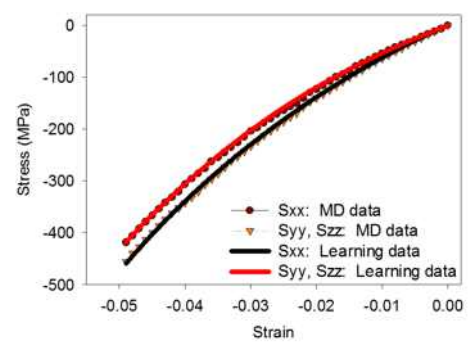
(a) $\epsilon_x : \epsilon_y = 1 : 2$



(b) $\epsilon_x : \epsilon_y = -1 : -2$



(c) $\epsilon_x : \epsilon_y : \epsilon_z = 0.5 : 1 : 1$



(d) $\epsilon_x : \epsilon_y : \epsilon_z = -0.5 : -1 : -1$

Fig. C.3.2 Comparison of MD data and learning data under the conditions indicated in (a), (b), (c), and (d).

C.4 Numerical examples of the NN stochastic constitutive model

The corner brace model was used to investigate the hyperelastic behavior of complex 3-D structures. A schematic diagram showing the deformed state obtained with the NN model when stretching the right side of the structure in the same direction is shown in Fig. C.4.1 (a) and (b). We applied a force of 2 MN and used the FEM model to determine which element presents the most variation and which element experiences the most stress. The largest variation was calculated to occur at point A, and the displacement of point A was determined in the form of a probability function according to the proposed stochastic NN constitutive model. The displacement probability function of the tip represents a normal distribution with a standard deviation of 0.038 based on the mean value of 0.227 (m), as illustrated in Fig. C.4.2 (a). In particular, the mean value and deviation value are indicated by blue and green circles, respectively, on the graph. In addition, it was found that the displacement of point A was within the range of 0.189–0.265, which is within the 68.2% reliability range, as depicted by the green arrow in Fig. C.4.2 (a). The stochastic numerical results provide additional information compared to the existing solutions, which provide only the values obtained as a result of the analysis, by also providing a range of values based on reliability. The stress distribution of the FEM model is shown in Fig. C.4.2 (b), which shows the effect of applying force to the model. These results indicate that the highest level of stress is applied at point B.

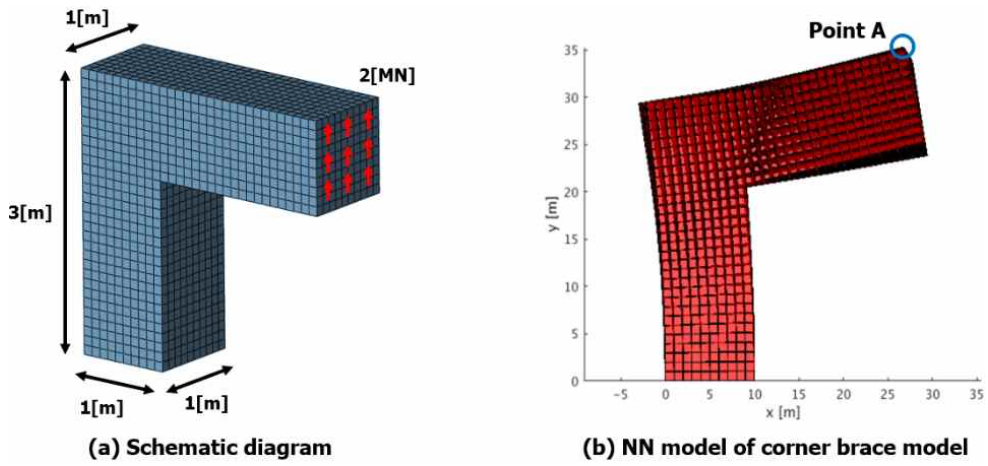


Fig. C.4.1 Corner brace model: (a) schematic diagram and (b) deformed state of NN model.

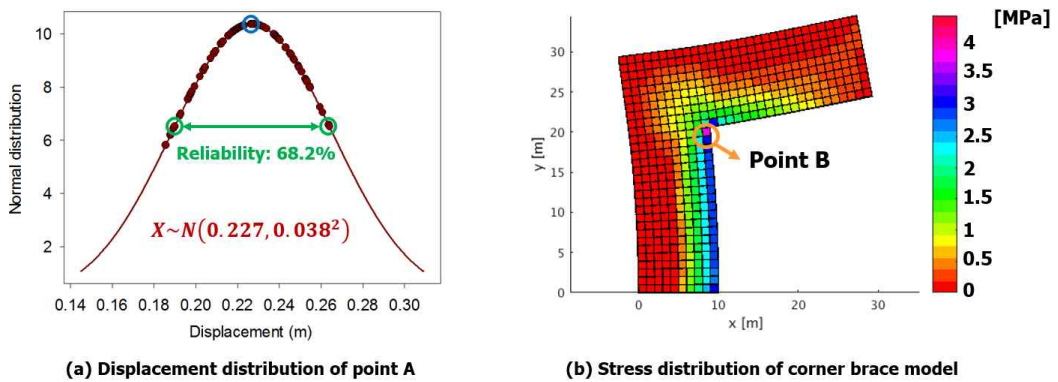


Fig. C.4.2 (a) Displacement distribution at point A and (b) stress distribution of the corner brace model.

C.5 Summary

In this paper, we proposed a constitutive model based on an NN that was employed for data-driven MD simulation to describe the hyperelastic behaviors of PS polymer. The material was modeled by MD simulations and massive datasets containing the hyperelastic responses were constructed. The results were obtained not only for monotonic loading conditions but also for combined loading conditions. The datasets generated by MD simulation were then used to determine the NN stress function and NN standard deviation function. We evaluated the performance of the NN functions by verifying their predictions of complex hyperelastic responses by excluding the loading data from the input data. The NN constitutive model described the hyperelastic behavior more accurately than the previous hyperelastic model based on the energy density function because the proposed model included the characteristics of the raw loading data. Based on the proposed numerical model, a hole-plate FEM model and a corner brace FEM model were constructed to investigate the hyperelastic responses of complex structures. In the case of the hole-plate model, the stress distribution of the model was similar for a small pulling force, whereas the stress values for the respective numerical models differed when a large pulling force was applied. The corner brace model enabled stochastic numerical results in the form of a normal distribution to be derived when using the NN constitutive model based on stochastic MD data, which provided confidence ranges for the analytical solutions.

Bibliography

- [1] Verbeeten WMH, Peters GWM, Baaijens FPT. Differential constitutive equations for polymer melts: The extended Pom-Pom model. *Journal of Rheology* 2001;**45**:823.
- [2] Likhtman AE, Graham RS. Simple constitutive equation for linear polymer melts derived from molecular theory: Rolie-Poly equation. *Journal of Non-Newtonian Fluid Mechanics* 2003;**114**:1-12.
- [3] Giesekus H. A simple constitutive equation for polymer fluids based on the concept of deformation-dependent tensorial mobility. *Journal of Non-Newtonian Fluid Mechanics* 1982;**11**:69-109.
- [4] Yang F, Ghosh S, Lee LJ. Molecular dynamics simulation based size and rate dependent constitutive model of polystyrene thin films. *Computational mechanics* 2012;**50**:169-184.
- [5] Mooney M. A theory of large elastic deformation. *Journal of applied physics* 1940;**11**:582.
- [6] Rivlin RS. Large elastic deformations of isotropic materials VI. Further results in the theory of torsion, shear and flexure. *Philosophical Transactions of the Royal Society of London. Series A, Mathematical and Physical Sciences* 1949;**242(845)**:173-195.
- [7] Ogden RW. Large deformation isotropic elasticity—on the correlation of theory and experiment for incompressible rubberlike solids. *Proceedings of the Royal Society of London. A. Mathematical and Physical Sciences* 1972;**326(1567)**:565-

584.

- [8] Yeoh OH. Some forms of the strain energy function for rubber. *Rubber Chemistry and Technology* 1993;**66(5)**:754-771.
- [9] Kim W, Chung H, Cho M. Anisotropic hyperelastic modeling for face-centered cubic and diamond cubic structures. *Computer Methods in Applied Mechanics and Engineering* 2015;**291**:216-239.
- [10] Kim B, Lee SB, Lee J, Cho S, Park H, Yeom S, Park SH. A comparison among Neo-Hookean model, Mooney-Rivlin model, and Ogden model for chloroprene rubber. *International journal of precision engineering and manufacturing* 2012;**13**:759-764.
- [11] Wang W, Zhao W, Nakamoto M, Schwarz M, He D, Zhang X, Zhao L, Syed A. Numerical model for understanding failure mechanism of back end of line (BEOL) in bump shear. *2020 IEEE 70th Electronic Components and Technology Conference* 2020.
- [12] Reuther GM, Albrecht J, Pufall R, Dudek R, Rzepka S. Determining adhesion of critical interfaces in microelectronics – a reverse Finite Element Modelling approach based on nanoindentation – Part 1, *Ieeexplore.iee.org* 2020.
- [13] Ogden RW, Saccomandi G, Sgura I. Fitting hyperelastic models to experimental data. *Computational mechanics* 2004;**34**:484-502.
- [14] Oscar LP. A new I1-based hyperelastic model for rubber elastic materials. *Comptes Rendus Mecanique* 2010;**338**:3-11.
- [15] Khajehsaeid H, Arghavani J, Naghdabadi R. A hyperelastic constitutive model

- for rubber-like materials. *European Journal of Mechanics A/Solids* 2013;**38**:144-151.
- [16] Sussman T, Bathe KJ. A model of incompressible isotropic hyperelastic material behavior using spline interpolations of tension–compression test data. *Communications in numerical methods in engineering* 2009;**25(1)**:53-63.
- [17] Shin H, Chang S, Yang S, Youn BD, Cho M. Statistical multiscale homogenization approach for analyzing polymer nanocomposites that include model inherent uncertainties of molecular dynamics simulations. *Composite Part B* 2016;**87**:120-131
- [18] Vu-Bac N, Lahmer T, Keitel H, Zhao J, Zhuang X, Rabczuk. Stochastic predictions of bulk properties of amorphous polyethylene based on molecular dynamics simulations. *Mechanics of Materials* 2014;**68**:70-84
- [19] Gao R, Li J, Ang AHS. Stochastic analysis of fatigue of concrete bridges. *Structure and Infrastructure Engineering* 2019;**15:7**:925-939.
- [20] Lemos T, Melo PA, Pinto JC. Stochastic modeling of polymer microstructure from residence time distribution. *Macromolecular Journals* 2015;**9**:259-270.
- [21] Latorre M, Montáns FJ. Extension of the Sussman–Bathe spline-based hyperelastic model to incompressible transversely isotropic materials. *Computers & Structures* 2013;**122**:13-26.
- [22] Latorre M, Montáns FJ. What-you-prescribe-is-what-you-get orthotropic hyperelasticity. *Computational Mechanics* 2014;**53(6)**:1279-1298.
- [23] Crespo J, Latorre M, Montáns FJ. WYPIWYG hyperelasticity for isotropic,

- compressible materials. *Computational Mechanics* 2017;**59(1)**:73-92.
- [24] Romero X, Latorre M, Montáns FJ. Determination of the WYPiWYG strain energy density of skin through finite element analysis of the experiments on circular specimens. *Finite Elements in Analysis and Design* 2017;**134**:1-15.
- [25] Nguyen LTK, Keip MA. A data-driven approach to nonlinear elasticity. *Computers & Structures* 2018;**194**:97-115.
- [26] Ghaboussi J, Garrett Jr JH, Wu X. Knowledge-based modeling of material behavior with neural networks. *Journal of engineering mechanics* 1991;**117(1)**:132-153.
- [27] Ghaboussi J, Sidarta DE. New nested adaptive neural networks (NANN) for constitutive modeling. *Computers and Geotechnics* 1998;**22(1)**:29-52.
- [28] Ghaboussi J, Pecknold DA, Zhang M, Haj-Ali RM. Autoprogressive training of neural network constitutive models. *International Journal for Numerical Methods in Engineering* 1998;**42(1)**:105-126.
- [29] Furukawa T, Yagawa G. Implicit constitutive modelling for viscoplasticity using neural networks. *International Journal for Numerical Methods in Engineering* 1998;**43(2)**:195-219.
- [30] Lefik M, Schrefler BA. Artificial neural network as an incremental non-linear constitutive model for a finite element code. *Computer methods in applied mechanics and engineering* 2003;**192**:3265-3283.
- [31] Hashash YMA, Jung S, Ghaboussi J. Numerical implementation of a neural network based material model in finite element analysis. *International Journal for*

numerical methods in engineering 2004;**59(7)**:989-1005.

[32] Yang H, Guo X, Tang S, Liu WK. Derivation of heterogeneous material laws via data-driven principal component expansions. *Computational Mechanics* 2019;**64**:365-379.

[33] Jung S, Ghaboussi J. Neural network constitutive model for rate-dependent materials. *Computers and Structures* 2006;**84**:955-963.

[34] Caylak I, Penner E, Dridger A, Mahnken R. Stochastic hyperelastic modeling considering dependency of material parameters. *Computational Mechanics* 2018;**62**:1273-1285.

[35] Vorselaars B, Lyulin AV, Michels MAJ. Deforming glassy polystyrene: Influence of pressure, thermal history, and deformation mode on yielding and hardening. *The journal of chemical physics* 2009;**130(074905)**.

[36] Harmandaris VA, Adhikari NP, van der Vegt NFA, Kremer K. Hierarchical modeling of polystyrene: From atomistic to coarse-grained simulations. *Macromolecules* 2006;**39**:6709-6719.

[37] Mondello M, Yang HJ, Furuya H, Roe RJ. Molecular dynamics simulation of atactic polystyrene. 1. Comparison with x-ray scattering data. *Macromolecules* 1994;**27**:3566-3574.

[38] Shin H, Choi J, Cho M. An efficient multiscale homogenization modeling approach to describe hyperelastic behavior of polymer nanocomposites. *Composites Science and Technology* 2019;**175**:128-134.

[39] Kim S, Ryu J, Cho M. Numerically generated tangent stiffness matrices using

the complex variable derivative method for nonlinear structural analysis. *Computer Methods in Applied Mechanics and Engineering* 2011;**200**:403-413.

[40] Sun W, Chaikof EL, Levenston ME. Numerical approximation of tangent moduli for finite element implementations of nonlinear hyperelastic material models. *Journal of Biomechanical Engineering* 2008;**130**(6).

[41] Kim H, Cho M. Study on the design sensitivity analysis based on complex variable in eigenvalue problem. *Finite element analysis and design* 2009-**329**(1)-84-95.

[42] Material Properties of Polystyrene and Poly(methyl methacrylate)(PMMA) Microspheres. Tech Support Doc 0021.

<https://www.bangslabs.com/sites/default/files/imce/docs/TSD%200021%20Material%20Properties%20Web.pdf>

국문 요약

본 논문에서는 소재 물성 및 계면 접합 조건의 불확실성을 고려한 적층 웨이퍼 구조의 파단 거동을 규정하기 위해 통계 기반 웨이퍼 파괴 모델을 제안하였습니다. 웨이퍼 필름은 제조 과정에서 반복되는 가열 사이클 공정, 기관 산화, X선 노출 등 다양한 외부 환경에 노출된다. 이러한 외부 요인으로 인해 불량 원인을 알기 어려운 웨이퍼 기관에서 다양한 계면 파손 현상이 관찰됩니다. 따라서 웨이퍼 필름의 파단 메커니즘을 규명하는 것이 중요하며, 웨이퍼 필름의 파손률 또한 반도체 산업에서 상당한 문제가 되고 있습니다. 그러나 웨이퍼 필름의 파단 분석을 위한 실험 수행에는 여러 어려움이 있습니다. 따라서 컴퓨터 시뮬레이션을 기반으로 웨이퍼 파단 현상을 분석하기 위한 많은 연구가 진행되고 있으며, 특히 파단 해석은 주로 **cohesive zone model**을 통해 이루어지고 있습니다. 그러나 기존의 해석 모델들은 거시적 규모의 실험 데이터를 기반으로 구축되었기 때문에 나노 스케일에서 관찰되는 계면 접합 조건을 정확하게 반영하는 것이 어렵습니다. 또한, 층상 웨이퍼 구조의 두께가 매우 얇기 때문에 각 층 구조가 나노 스케일 구조로 되어 있고, 그로 인해 웨이퍼를 구성하는 물질이 불균일하게 형성됩니다. 그 결과 웨이퍼 재료의 물성에 대한 불확실성이 발생하고,

재료 간의 계면 특성에도 불확실성이 발생하게 됩니다. 이러한 불확실성은 전체 웨이퍼 구조의 파괴에 큰 영향을 미치므로, 이를 고려하여 웨이퍼 필름의 파단 해석을 분석할 필요가 있다. 또한 불확실성을 고려한 통계 기반 파괴 해석은 최근 웨이퍼 구조는 물론 콘크리트, 고분자 복합재료 등 다양한 복합재료에서 연구되고 있는 주요 이슈입니다.

본 연구에서는 나노 스케일에서 재료 및 계면 특성의 불확실성을 해결하기 위해 통계 기반 분자 역학 분석 모델을 제시하였습니다. 통계적 분석을 통해 웨이퍼 소재의 열역학적 특성 및 계면 파단 특성을 정규분포를 기반으로 제시할 수 있습니다. 또한 Monte-Carlo 시뮬레이션을 통해 적층 웨이퍼 구조의 계면에서 통계적 파괴 기준을 새롭게 제안하였습니다. 해당 물성들의 확률 분포는 분자 역학 시뮬레이션을 통해 웨이퍼 재료 및 계면 특성의 불확실성을 고려하여 계산됩니다. 물성들의 확률 분포를 바탕으로 cohesive zone model을 통해 유한요소 파괴 모델을 구축하였습니다. 웨이퍼 필름에 대한 재료 및 계면 특성의 불확실성을 반영하기 위해 통계적 다중 스케일 브리징 방법을 새롭게 제안하였습니다. 소재 물성 및 계면 파괴 특성의 각기 다른 통계 기반 분포를 함께 고려하기 위해 본 연구에서는 Monte-Carlo 시뮬레이션을 수행하였고 그 결과 구축한 통계 기반 웨이퍼 파괴 해석 모델을 새로 제안합니다. 통계 기반 수치 해석 결과는 신뢰성

한계를 내포하는 수치 해석 값 뿐만 아니라 웨이퍼 시스템의 오차 범위 및 수율을 제공합니다.

가장 일반적으로 사용되는 3차원 판 모델을 통해 적층 웨이퍼 구조의 시뮬레이션 모델을 구축하였고, 이를 통해 본 연구에서 제시하는 통계 기반 파괴 해석 모델을 perfect bonding model과 cohesive zone model의 기존 웨이퍼 파손 모델과 비교하였습니다. 각 웨이퍼 파괴 모델에 대해 열 응력 하에서 변형 정도와 파괴 거동을 비교하여 제시하였습니다. 통계적 웨이퍼 파단 모델은 해석 값을 정규분포의 형태로 제시할 수 있으며 이를 통해 다른 모델과 달리 적층 웨이퍼 구조의 수율을 예측할 수 있습니다. 또한 실험 데이터와의 비교를 통해 제안한 통계 기반 파괴 해석 모델이 기존 파괴 해석 모델보다 웨이퍼 필름의 파단을 보다 정확하게 예측할 수 있음을 확인하였습니다.